UNIVERSITÀ DEGLI STUDI DI NAPOLI "FEDERICO II"
FACOLTÀ DI INGEGNERIA

Dottorato di ricerca in "Ingegneria Aerospaziale, Navale e della Qualità" – XXIV Ciclo

Settore scientifico disciplinare ING-IND/05:
Impianti e Sistemi Aerospaziali

Vision based strategies for implementing Sense and Avoid capabilities onboard Unmanned Aerial Systems

Ing. Lidia Forlenza

Tutors:

Ch.mo Prof. Ing. Antonio Moccia

Ch.mo Prof. Ing. Domenico Accardo

Coordinatore:

Ch.mo Prof. Ing. Antonio Moccia

To understand this for sense
it is not required that a man should be a geometrician or a logician,
but that he should be mad.

(Per comprendere il significato di ciò,
non si chiede che un uomo sia un geometra o un logico,
ma che sia matto.)

Thomas Hobbes (1588-1679)

Ai miei quattro AMORI,

con tanto AMORE

Abstract

Current research activities are worked out to develop fully autonomous unmanned platform systems, provided with Sense and Avoid technologies in order to achieve the access to the National Airspace System (NAS), flying with manned airplanes. The TECVOl project is set in this framework, aiming at developing an autonomous prototypal Unmanned Aerial Vehicle which performs Detect Sense and Avoid functionalities, by means of an integrated sensors package, composed by a pulsed radar and four electro-optical cameras, two visible and two Infra-Red. This project is carried out by the Italian Aerospace Research Center in collaboration with the Department of Aerospace Engineering of the University of Naples "Federico II", which has been involved in the developing of the Obstacle Detection and IDentification system.

Thus, this thesis concerns the image processing technique customized for the Sense and Avoid applications in the TECVOL project, where the EO system has an auxiliary role to radar, which is the main sensor. In particular, the panchromatic camera performs the aiding function of object detection, in order to increase accuracy and data rate performance of radar system. Therefore, the thesis describes the implemented steps to evaluate the most suitable panchromatic camera image processing technique for our applications, the test strategies adopted to study its performance and the analysis conducted to optimize it in terms of false alarms, missed detections and detection range. Finally, results from the tests will be explained, and they will demonstrate that the Electro-Optical sensor is beneficial to the overall Detect Sense and Avoid system; in fact it is able to improve upon it, in terms of object detection and tracking performance.

Keywords: Unmanned Aerial Systems, Collision Avoidance, Electro-Optical Systems, Image Processing Algorithm, Multisensor Tracking.

Acknowledgements

This is my chance to thank a lot of people I have met and I have lived with, during these short but very intensive three years. First of all, thanks to my tutors, Professor Moccia and the Engineer Domenico Accardo, who have given me the possibility to begin and to carry on the PhD adventure, during which I have experienced the fantastic world of the Research. Consequently, my thanks enlarge to all Department of Aerospace Systems staff: my appreciations go to Professor Michele Grassi, for his happiness and kindness and to the Engineer Giancarlo Rufino, for his willingness and sensitiveness. Moreover, I cannot forget my two friends Giancarmine Fasano and Alfredo Renga, who have been my two robust shoulders of these three years, also during rainstorms and floods, as Giancarmine knows.

Thus, I can dedicate now some rows to my loves, just to remember they have been fundamental also during these three years, other than all my life. Thank you Papà, because you always believe in me, also when I don't do the same and you allow me to see always the positive sides of things: you are my light. Thanks Mamma, because I know you are in each moment I need; I feel you always are near me, even when we don't talk for days: you are my strength. Furthermore, my little sis is my pride…I know, you look at me, but you don't know that I look at you silently, and I observe how many progresses you conquer each single day…you are simply fantastic! Moreover, I would like to thank my enlarged family: many kisses to Raffaella, Amelia and Raimondo, who contribute to increase my strength, because they are always ready to listen to me and talk about everything I need…thank you very very much… I feel your support more than you know!

I dedicate few words to my grandmother…who is the rock of my life…and finally I can write about us! Thank You my Love to be always with me, independently on the distances and the time of day… these three years have been very intensive and rich of adventures that we have been able to afford with audacity and smartness… do you know why? It is very simple… simple because we are together and everything one of us does…he is never alone, but he has the double strength of all common people…we are special because we are two…what about the future?? To keep on doing in that way… with the protection of who looks after us from the sky (I really feel Him)!!

Thanks to Everyone, with sincere love… ***Lidia***

Contents

Introduction

In the last decades many autonomous and tele-operated vehicles for field robotics have been developed, including wheeled, tracked and legged vehicles. However, in many cases, ground vehicles have significant inherent limitations to access to the desired locations due to the characteristics of the terrain and the presence of obstacles that cannot be avoided. In these cases aerial vehicles are the natural way to approach the objective to get information or even to perform some actions such as the deployment of instrumentation. Then, aerial robotics seems a useful approach to perform tasks such as data and image acquisition of targets and affected areas, localization of targets, tracking, map building and others.

In this framework, Unmanned Aerial Vehicles (UAVs) represent an important solution as in the military as in the civil fields, concerning a wide scenario of scientific applications, such as terrain and utilities inspection, disaster monitoring, environmental surveillance, search and rescue, law enforcement, aerial mapping, traffic surveillance, and cinematography. Moreover, in the last years UAVs improved their autonomy both in energy and information processing.

However, the development of autonomous aerial robotic vehicles involves many problems related to limited payload, safety requirements, flight endurance and others [1].

In particular, the most common challenges for the full autonomy UAVs development can be synthesized in the following points:

- Decisional autonomy;
- Guidance, Navigation and Control (GNC) system and payload integration;
- Operational safety and security;
- Certification;
- All-weather all time operational capability;
- Obstacles Sense And Avoid (SAA);
- Data processing.

Many projects, related to the development of autonomous aerospace systems, are carried out all over the world, involving research centers and universities of USA, Europe, Japan and Australia; all of them present different objectives and fields of application that are schematized in figure 1.

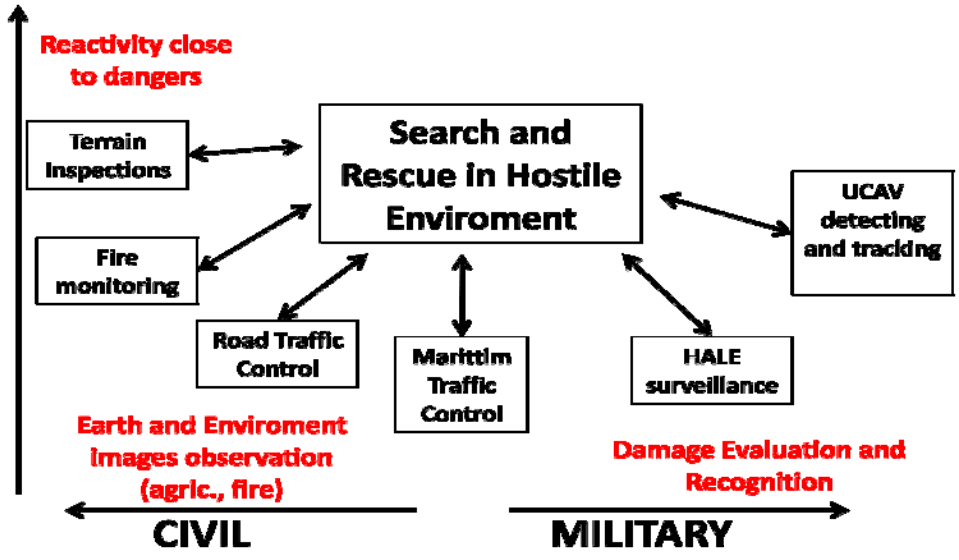

Figure I.1 Autonomous Aerospace Systems Applications: common challenges and comparison

However, the UAV support in hostile environment is a great advantage for the human life, as in surveillance as in rescue missions [2]. Indeed, the University of Madrid is carrying on a project concerning a strategy to track and describe the boundary of an environment by means of images came from an UAV with a visible camera installed onboard [3]; moreover the problem of extinguishing forest fires is being analyzed by the college of Engineering of Chennai which proposes a quadrant of nodes for detecting and extinguishing forest fires using UAV Networks [4].

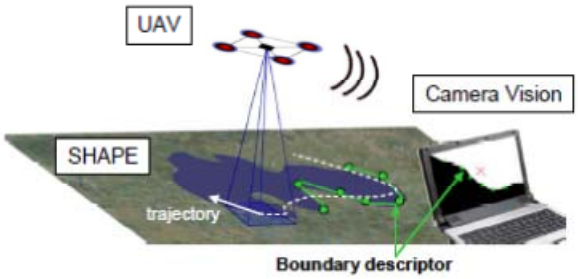

Figure I.2 Boundary Identification by UAV

As regards the search and rescue support, it's important to mention the Massachusetts Institute of Technology (MIT) contribution with its Collaborative Mission Planning, Autonomy and Control Technology (COMPACT) project which is characterized by unmanned surface and aerial systems cooperation that share information of failure detection and position in order to have the immediate support and supplying human intervention [5]. In parallel the Georgia Institute of Technology is developing a Disaster Relief and Emergency Response (DRER) services based on UAVs network as in the military as in the civil sector [6].

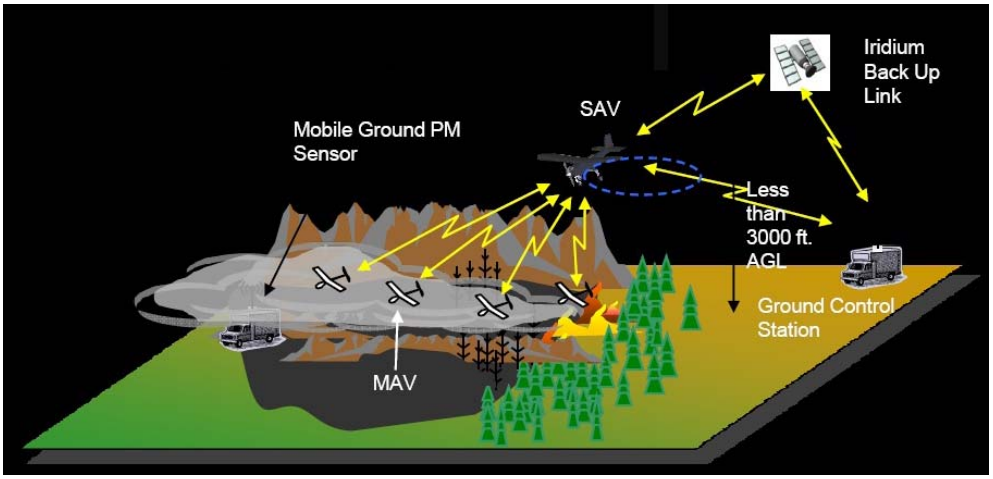

Figure I.3 Cooperation between Unmanned and Manned Vehicles for improving fire behavior forecasts and predicting smoke and fume impingement

UAVs are often used in agricultural mapping applications, such as by the Unmanned Aircraft Systems Engineering (UASE) team of the University of Dakota which is developing a precision agriculture imaging payload flown in a Unmanned Aerospace System (UAS), in order to have a prescription map for an agricultural field and to provide cost effective information about a large geographic region [7].

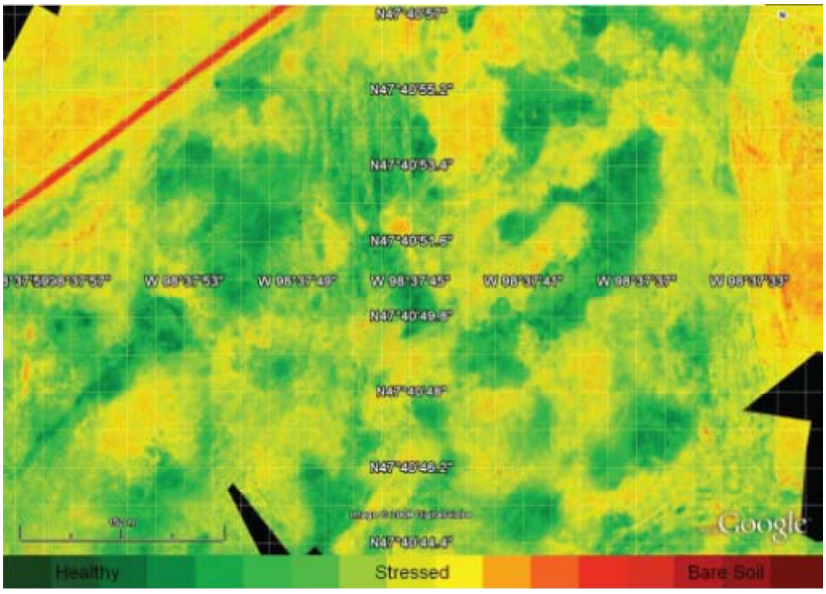

Figure I.4 Geo-referenced mosaic of relative crop health (final product)

However, most current research activities concern the developing of autonomous function for aerial vehicles due to

their strong support to human missions; indeed UAV platforms can operate in a wide range of environmental scenarios, even those very dangerous for human life.

The last step to be gained for the full unmanned aircraft autonomy is to allow them to operate in the National Airspace System (NAS), mixed with manned aircraft. The Federal Aviation Administration (FAA) is investigating ways to regulate their integration in the civil airspace in order to accommodate their growth in numbers and applications [8].

A major issue in accepting UAS in manned airspace is the ability to avoid collision with obstacles, most importantly, manned aircrafts. Thus, many research experiments are attempting to develop SAA solutions for airborne unmanned platforms, all of them are based on the FAA Regulation 7610.4 [9], which states that remotely operated aircraft must provide "… an equivalent level of safety, comparable to see-and-avoid requirements for manned aircrafts" in order to operate like manned aircrafts in the NAS. The capability must be effective against all air traffic, with or without active, transponder-based collision avoidance systems. Currently no Remotely Operated Aircraft (ROA) "sense and avoid" capability exists, but already many airborne platforms, manned and unmanned, are being customized to integrate and to test the SAA technology.

I.1 Why the Sense and Avoid Technology?

The research based on the SAA technology is intentionally focused on small UAS missions as the driver, with a payload limitation of ounces to pounds. There is a reasonable expectation that a solution maybe scalable to larger UAS; though differing missions and conditions may affect the scalability. Rather than scaling up, many approaches today are looking at large UAS and the possible sensor solutions and hoping to scale the solution down. The operating environment for these UAS is expected to be civil, uncontrolled, Visual

Flight Rules (VFR) airspace. UAS operation in this airspace could encounter a variety of airborne targets such as small manned aircraft without transponders. Therefore this research examines the sensor-based non-cooperative solutions, not the transponder-based cooperative methods. However, in order to realize a collision avoidance system (CAS), a variety of sensors have to be taken into account, such as the Traffic alert and Collision Avoidance System (TCAS), Automatic Dependent Surveillance-Broadcast (ADS-B), electro-optical (EO) and Infra-Red (IR) systems, and radar. TCAS and ADS-B provide a satisfactory means of sensing transponder-equipped aircraft but they lack the ability to detect aircrafts that are not equipped with a transponder; on the other hand, EO, IR and radar sensors are appealing solutions for detecting traffic because they do not require that intruders have special equipage [10].

Figure 5, from AeroSafety World Magazine [11], clarifies the meaning of SAA in the overall Air Traffic Control (ATC) scenario and illustrates that the Detect Sense & Avoid (DS&A) technology is the last obstacle before the aerial collision.

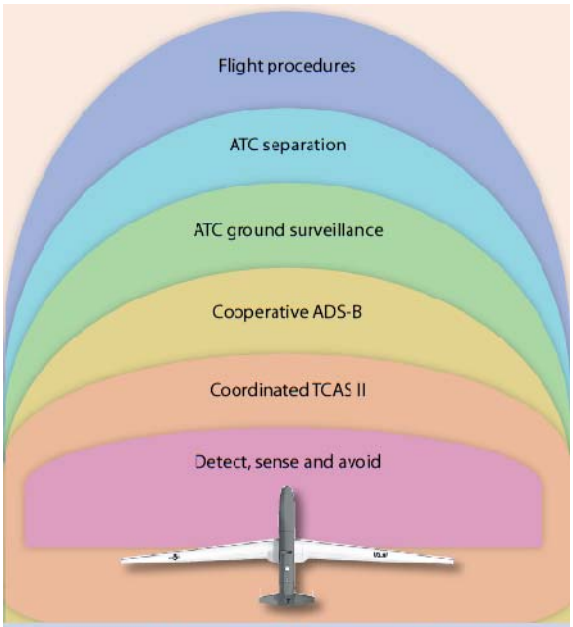

Flight procedures	For example, under FAA visual flight rules, a magnetic course/ ground track of 180–359 degrees requires flight at even thousands mean sea level (MSL) plus 500 ft if more than 3,000 ft above the surface but below 18,000 ft MSL.
ATC separation	Controllers provide route clearances, traffic information and radar vectors for aircraft separation.
ATC ground surveillance	Responses from interrogations of aircraft transponders are integrated with targets on ATC ground radar displays. ADS-B transmissions received by ATC then could be broadcast to aircraft equipped to display traffic information service–broadcast targets in the cockpit.
ADS-B	The 1090-MHz extended squitter version of this technology offers 40-nm (74-km) range in high-density environments and 90-nm (167-km) range in low-density environments.
TCAS II	Traffic advisory begins at distances as far as 40 nm; resolution advisory occurs 25–45 seconds before the closest point of approach.
Detect, sense and avoid	Technology under development would correlate and fuse inputs from DSA sensors, TCAS II and ADS-B to alert UAS pilots and enable the UA to automatically perform the appropriate collision-avoidance maneuver.

ATC = air traffic control; ADS-B = automatic dependent surveillance–broadcast; FAA = U.S. Federal Aviation Administration; DSA = detect, sense and avoid; UAS = unmanned aircraft system

Source: Northrop Grumman Integrated Systems

Figure I.5 UAS Safety Layers Under Study for Collision Avoidance

Because of the limitations of platforms and sensors, it is expected that the UASs must deal with very short timeframes to react, for sensing and avoiding fixed and moving obstacles. The following flow diagram shows the basic operations of a reactive Sense and Avoid solution.

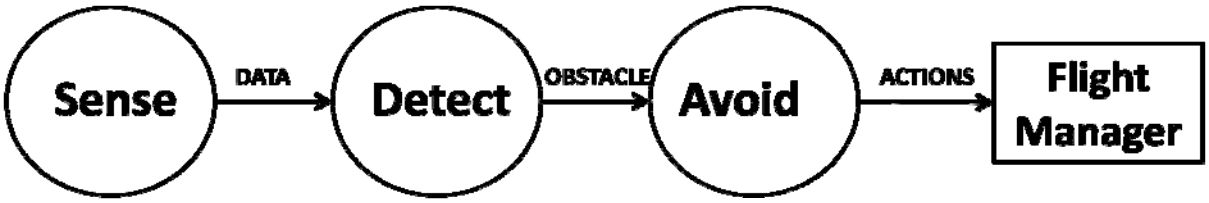

Figure I.6 Flow Diagram for Reactive Sense and Avoid

I.2 UAV platforms for Sense and Avoid technologies

To support the SAA testing many airborne platforms have been experimented, both fixed and rotary wing, which are representative of typical UAS expected to see increased use in the NAS. Additionally, each has unique advantages suited to conducting experimentation. Rotary wing platforms have the option of full three dimensional control of velocity; fixed wing platforms allow easily repeatable encounter geometries and typically longer loiter times for extended data collection

However, as regards fixed wing aircrafts, Northrop Grumman and the US government have launched the Broad Area Maritime Surveillance (BAMS) program (2008), which involves the developing of a Sense and Avoid system composed by Radar as primary sensor and EO system as auxiliary ones, in order to meet requirements still being developed by the Federal Aviation Administration and to be integrated on the Global Hawk RQ-4N [12]. The latter is a High Altitude Long Endurance (HALE) UAV which reaches 65000 ft of altitude, 35 hours of flight and can bear up to 1900 lbs.

Another UAV, considered suitable for installing SAA system onboard, is the General Atomics' Predator [13], which is another HALE platform able to fly for 30 - 40 hours at 27000 ft with 450 lbs of payload. The prototype technology is being developed by the US Air Force Research Laboratory's [AFRL] sensors directorate and will be based on only optical sensors

and processing systems jointly developed by AFRL and Defence Research Associates.

At last, another aircraft thought to be ideal for SAA technology is the Tactical UAV Pioneer that flies at 15000 ft for 5-6- hours with 25 kg payload.

Figure I.7 Northrop Grumman's Global Hawk

Figure I.8 General Atomics' Predator

Figure I.9 AAI Pioneer

Furthermore, there are many rotary wing Vertical Take-off and Landing (VTOL) platforms selected for integrating SAA technologies. The MITRE Corporation has chosen two medium-size helicopters manufactured by Miniature Aircraft – the GasXcell and the SpectraG [10]. The first is equipped with a visible camera and a laser range finder; whilst the second has only electro-optical sensors. Their advantage is the capability of carrying substantial payloads and of stopping and hovering when confronting a target.

Figure I.10 GasXcell

Figure I.11 SpectraG

Moreover, the Yamaha R50 and Rmax are solutions commonly adopted in current SAA research activities, due to their ability to maintain the aerial vehicle in hovering and to attain long flight endurance and increased payload requirements (1 hour of flight with 24 kg of payload). In particular, the Robotics Institute at Carnegie Mellon University (CMU) has conducted since the early nineties an autonomous helicopter project based on the Yamaha R50 platform [14], as well as the University of Linkoping, Europe, whose WITAS project uses the Yamaha Rmax helicopter as experimental platform [15]; in both cases the UAV is equipped with electro-optical sensors. Furthermore, the "Office National d'Etudes et de Recherches Aéronautiques" (ONERA) is carrying on the "Recherche Et Sauvetage par Système Autonome Coopérant" (ReSSAC) project which involves the Yamaha Rmax for testing several UAV autonomous capabilities other than sense and avoid, basing on data acquired from visible images (take-off, landing, mission control, intruder vehicles detection and tracking) [16].

Figure I.12 Yamaha Rmax

I.3 Thesis objectives and outline

This thesis has been developed in the framework of a SAA research project, carried out by the Italian Aerospace Research Center (CIRA) in collaboration with the Department of Aerospace Engineering (DIAS) of the University of Naples "Federico II". In particular, it concerns the implementing and testing of image processing techniques for the visible cameras, which provide the "sense" function of the overall DSAA system, installed onboard a Very Light Aircraft (VLA), customized for our research studies.

However, all these aspects will be treated in detail in the thesis, on the basis of the following outline.

Chapter 1 is dedicated more in detail to the sense and avoid problem, focusing on the collision avoidance requirements and the description of several possible sensor choices and architectures, pointing out their advantages, disadvantages, in terms of power, accuracy, data rate and payload performance.

Chapter 2 aims at describing the designed anti-collision system for the CIRA project. In particular, the experimental

VLA platform and its overall DS&A system are presented. The setup will be explained as from the architectural as from the hardware point of view.

The detailed illustration of the selected EO units for the CIRA project is provided by chapter 3; moreover a section is dedicated to the description of the alignment of the electro-optical sensors with the inertial unit of the aerial experimental platform. Furthermore the main image processing algorithm topics for implementing the obstacle detection function are pointed out.

In chapter 5, the most common image processing techniques for object detection applications are presented and compared, in terms of computation time and accuracy; however, several foreign research experiences are deepened, because reference applications for our research field.

Chapter 8 is dedicated to the description of the Hardware-in-The-Loop (HWIL) system, realized to support the flying experimental platform. It has been set up in the DIAS laboratory in order to test the detection by sensors, data fusion and tracking performance of the real DS&A system, installed onboard the VLA. However it is characterized by simulator and real components, such as the visible camera.

Furthermore, chapter 7 focuses on the selected image processing technique performance. In particular its implementation on several images acquired during flight tests is illustrated, together with some image processing critical issues, such as sun light and horizon line presence. At last the managing of those issues is explained and the assessed algorithm performance is schematically presented.

Finally, conclusions and further research activities are pointed out in the last chapter.

Chapter 1

Requirements for Sense & Avoid Systems

In order to fulfill the requirement of "equivalent levels of safety" [9], the design of a SAA system for UAV systems operating in non-segregated space has to verify some functional requirements, provided by North Atlantic Treaty Organization (NATO) in ref. 17. and by FAA in ref. 9.

However, these documents aim at providing specific requirements intended to be applied to the airborne SAA function, in order to achieve a "target level safety" comparable to that for manned aircrafts. Thus, the most stringent requirement facing unmanned aviation can be derived from the need for operations with Commercial Air Transport, which commands that the probability of a Mid-Air-Collision (P_{MAC}) must be equivalent to, or better than 5×10^{-9} per aircraft flight hour [17].

Indeed, for any Mid-Air-Collision (MAC) the following sequence of events have to happen:

- Two aircrafts are on a collision course;
- A failure in separation provision occurs;

- Simultaneously, there are both collision avoidance functions failures, UAV's and the other aircraft's.

Because of each event has a discrete probability of happening, the total P_{MAC} is the product of the probabilities of the above events and it is expressed by the relation (1):

$$P_{MAC} = P_{Collision\ Course} \times P_{Separation\ failure} \times P_{UAV\ Collision\ Avoidance\ failure} \times P_{Conflicting\ Aircraft\ Collision\ Avoidance\ failure} \quad (1)$$

where $P_{collision\ course}$ is the probability of collision dependant on air traffic density; $P_{separation\ failure}$ is the probability of loss of separation (by either ATC or Designed UAV Operator (DUO)); $P_{UAV\ Collision\ Avoidance}$ failure and $P_{conflicting\ aircraft\ Collision\ Avoidance\ failure}$ are the probabilities of the failure of the collision avoidance function of UAV and conflicting aircraft respectively.

Despite of the high number of events which have to coexist to cause a MAC, many aerial accidents have been reported in literature due to the occurring of some failures above mentioned. However, the U.S. National Transportation Safety Board (NTSB) Public Forum on UAS has described some UAS accident, such as the crash of a Predator B UAS operated by U.S. Customs and Border Protection near Nogales, Arizona [18]. Concerning that event, the NTSB stated that several factors related to pilot training and proficiency in dealing with emergency situations contributed to the accident". Furthermore, the NTSB reported the crash of a Raytheon Cobra, a small UAS, in Whetstone, Arizona, defining the main cause of the accident a student pilot's failure to follow proper procedures; consequently it resulted in loss of aircraft control [19].

1.1 Sense & Avoid Systems Functions

As already stated, the main goal of any SAA system is to provide sufficient information to maintain aircraft separation and collision avoidance functions.

However, the separation provision is the routine act of keeping aircraft apart, in order to mitigate the risk of collision, and its responsibility lies either the ATC controller or the DUO; on the other hand, collision avoidance reacts when the separation provision has failed and imminent risk of collision exists. It is applicable at all times, in any class of airspace under any flight rules.

In order to satisfy those functionalities, an Obstacle Detection and Tracking System, designed for Autonomous Collision Avoidance, has to fulfill some specifications, such as the minimum range of initial detection, size and shape of the Field Of Regard (FOR), error detection of intruder position, measurements rates and latencies.

This anti-collision sensor system performance is summarized on a quantity level in table 1, where also the intruder position resolution is indicated.

Table 1.1 Requirements for Collision Avoidance System

PARAMETER	VALUE
FOR in azimuth	-110° - +110°
FOR in elevation	-15° - +15°
Range resolution	20 m
Azimuth resolution	0.27°
Elevation resolution	0.27°
Minimum allowed time-to-collision	19 s
Data Rate	10 Hz

Thus, the minimum range of initial detection is calculable from the minimum-time-to-collision. In fact, it is a linear function of both the minimum time to collision that still permits a collision avoidance maneuver to be completed, and of the maximum frontal approaching speed V_{MAX}. However, considering two aircrafts in frontal collision trajectory flying at the maximum allowed speed, that is 463 m/h [9], this leads to a V_{MAX} of about 926 km/h (500 kts). Consequently, the minimum range for a safe initial detection in mid-air conditions is calculated by:

$$R_{MIN,AVOID} = V_{MAX} \times T_{MIN,AVOID} \quad (2)$$

From which, it results $R_{MIN,AVOID}$= 4.9 km.

As regards the FOR, it must be similar to the one of manned aircraft. It is shaped as a rectangular spherical sector with a depth that is equal to the sphere radius and two angular spans given by azimuth α and elevation β angles. Indeed, the depth must be sized so that it is equal to $R_{MIN,AVOID}$. Azimuth and elevation angular spans must be the same of manned aircraft in order to keep the same safety level, as mentioned in ref. 17, i.e. the recommended size is a minimum of ± 110° horizontally with respect to the longitudinal axis of the UAV, a minimum of ± 15° vertically with respect to the flight path at normal cruise speed, and provides sufficient coverage to enable separation of conflicting air traffic during expected maneuvers. Nonetheless, smaller intervals can be assumed as a near term compromise, as stated in ref. 21, where α ϵ[-90°, +90°] and β ϵ[-10°, +10°] are proposed.

Moreover, the error in the determination of intruder position and speed with respect to own aircraft must be limited so that false alarms and missed detections of collisions are restricted within a desired level. A collision threat is defined when two aircrafts fly closer than a safety distance S

that is stated by aeronautical regulations (500 ft) [9]. As a consequence, a collision in the near future can be predicted when the relative speed vector between own aircraft and intruder crosses the "safety bubble", i.e. a sphere that is centered on the current relative position of the intruder aircraft and it has a radius equal to S. Thus, the performance of obstacle detection and tracking system can be synthetically measured evaluating the accuracy in estimating the distance at Closest Point of Approach (CPA).

1.2 Sensors suit for SAA technologies

Any sensor technology for sense-and-avoid application is characterized by the following parameters:

- Maximum operational range and range resolution (accuracy of measurement);
- Maximum angular Field Of View (FOV) (azimuth and elevation) and angular resolution;
- Frame rate corresponding to the time interval at which the measurements are updated.

The first sensor technologies distinction consists in their classification into active and passive sensing. Their main difference consists in their employing of energy, in order to sense objects of the environment. In particular, the active sensors are based on acoustic and electromagnetic radiations to provide direct measurement of range, by measuring time-of-flight delays of back scattered reflection and they are characterized by a radar-like configuration. On the other hand, the passive sensing receives energy from the environment, including the object, by devices such as standard cameras, and consequently a 2D map of the 3D environment can be constructed. Moreover, range of objects can then be calculated by using multiple images, applying the stereoscopic technique, or by comparing sequencing images taken by the same

camera and processed by some particular image processing methods, such as the corner detection, the optical flow [22 - 25].

The choice of the best sensor system suitable for a SAA technology is complex, because it takes into account many aspects, such as weight and power requirements, computational load, UAS capabilities and payload constraints. Table 2 synthesized the sensor comparison and attributes.

Table 1.2 Active and Passive Sensors: Comparison and Characteristics

	ACTIVE	**PASSIVE**
POWER	High	Low
Field Of Regard	Little	Extended
RESOLUTION	Low	High
COMPUTATIONAL LOAD	Light	Heavy
SYSTEMS OF EXAMPLE	Radar, Ladar	EO, Thermal systems

However, let us observe that the main advantages guaranteed by active sensors are their capability of providing range measurement directly and that the post-processing efforts are minimal, but, on the other hand, they require high power supply, because they employ scanning mechanism to perform angular measurements, adding complexity to the platform. Moreover, the angular resolution is determined by the size of the antenna in relation to the wavelength of radiation, therefore shorter wavelengths (IR) are preferable in order to reduce the size of the antenna and the weight platform. Whereas, shorter wavelengths are more sensitive to fog and dust, limiting operation in good visibility conditions.

The interplay between sensor system complexity and post-processing requirements is reverse for passive, indirect sensor technologies. A traditional camera operating in visible

or IR frequencies is compact, provides angular information directly (no scanning) and has low power requirement. On the other hand, the ability to estimate range information is often limited and requires sophisticated computation, sometimes difficult to run in real-time applications.

In conclusion, the best approach to sensing may very well be a combination of sensing technologies. It will be particularly useful if the sensor payloads that are already onboard the UAS can be leveraged to provide part of the sense-and-avoid functionality.

1.3 Sensing Solutions: international experience

Many sensor combinations have been experienced all over the world. They range from standalone electro-optical systems [26-32] to standalone radars or integrated radars and EO [20,33-35], and EO systems and/or radars integrated with collaborative systems such as TCAS or ADS-B [36,37].

In particular, as regards the first type of approach, the Defense Research Associates, Inc. (DRA) and the Air Force Research Laboratory (AFRL/SNJT) have developed a SAA technology based on silicon charge couple device (CCD) and passive moving target detection algorithms [26]. They used an Aerostar UAV as demonstration platform and a Beech Bonanza as intruder aircraft; after flight test sessions, they learned that image processing algorithms was strongly sensitive to environmental conditions, producing thousands of false tracks; however they need intense improvements, so that standalone EO systems could become more reliable air traffic detection sensors.

Figure 1. 13 Air Traffic Detection Sensor System Hardware of DRA and AFRL/SNJT

Better results have been obtained by the Australian Research Centre for Aerospace Automation (ARCAA) aerial robotics [30]. They mounted the camera system on-board a Cessna 172 aircraft, and experimented good detection performance in terms of correct detections and false alarms, even if the detection range is less than 1 km.

(a) (b)

Figure 1.14 (a) ARCAA Airborne Systems Laboratory Cessna 172 aircraft; (b) Dual camera system showing forward and downward pointing cameras

An example of the second type of approach has been tested by the Thales Airborne Systems [35] which has simulated the joint Radar/EO tracking, demonstrating that is more accurate than the radar-only solution.

A solution based on collaborative systems has been examined by MITRE [37]. In particular its work studies the potential sensitivities and shortcomings of the TCAS collision avoidance system for unmanned aircraft. Results derived from a Monte Carlo safety simulations demonstrated that to evaluate TCAS performance, various aspects of the SAA system have to be taken into account, such as sensor performance, human performance, vehicle maneuver dynamics, and encounter characteristics. This last model will depend strongly upon the type of mission profiles to be flown, and the airspace traffic characteristics.

Chapter 2

CIRA TECVOL Project

Another Sense & Avoid project has been carrying out by the CIRA and the DIAS of the University of Naples "Federico II". In particular, they are developing a fully autonomous multi-sensor anti-collision system for UAVs, in the Technologies for Autonomous Flight (TECVOL) project. More in detail, TECVOL is set within the P.R.O.R.A. UAV program, which aims at developing a HALE UAV for civil application. Thus, TECVOL was born in order to realize the technologies needed to support the HALE UAV flight autonomy, being able to integrate the following functions:

- Autonomous Flight Path Execution
- Autonomous Approach and Landing
- Obstacle DS&A
- Autonomous Runway Search and Lock
- Enhanced Remote Piloting

However, in the TECVOL preliminary studies [38], a multi-sensor configuration was selected between the several sensing solution, already explained in the chapter before, in order to perform the obstacle detection and tacking function, constituted by either EO or radar systems, able to fulfill all SAA requirements, stated before.

2.1 Overall System Description

The overall DS&A TECVOL hardware is installed onboard an experimental flying platform, which is a customized version of TECNAM P92 Very Light Aircraft (VLA), named Flying Laboratory for Aeronautical REsearch (FLARE)(figure 2.1).

Figure 2.15 FLARE platform

It is constituted by two main units: the Obstacle Detection and Identification (ODID) and the Flight Control Computer (FCC). The first one is the obstacle sensing part of the overall system, which comprises a pulsed Ka-band radar, four EO sensors, a CPU devoted to image processing (IP-CPU), a CPU devoted to real-time tracking (RTT-CPU) by sensor data fusion. Thus, the second unit provides autonomous navigation and flight control by a set of navigation sensors (Attitude and Heading Reference System (AHRS), Laser Altimeter, Standalone GPS, Air Data Sensors). Moreover it comprises a Guidance Navigation and Control (GNC) Computer capable of processing obstacle dynamics and UAV navigation data in real-time to generate escape trajectories and the relevant commands for servos.

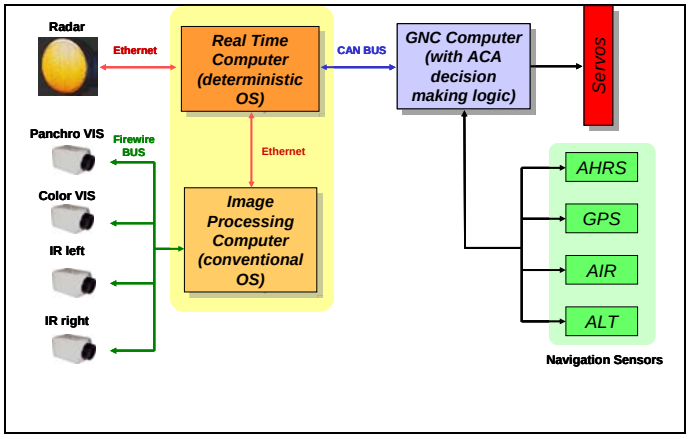

Figure 2.16 S&A system hardware architecture (OS: Operating System; ACA: Autonomous Collision Avoidance; AIR: AIR data sensors; ALT: laser ALTimeter).

Figure 2.2 illustrates more in detail each module characteristics and their connections. However, it's worth noticing that the RTT-CPU represents the interface between the two main units, by means of a deterministic Controller Area Network (CAN) bus. Therefore, the Autonomous Collision Avoidance (ACA) logic is based on two core algorithms [33]. Firstly, ODID runs the multi-sensor tracking software (SW), ensuring that the intruder's dynamics is properly followed and estimated. Secondly, the FCC performs the ACA decision making logic, on the basis of the ODID and GNC data, in order to handle collision conditions in real time and perform adequate evasive maneuvers.

The following figure is a scheme of the ACA functionalities, within the closed-loop control system. However, the reader can observe that the ODID outputs and the navigation data are the inputs to the ACA decision making algorithm; in particular, ODID module sends the intruder position and speed vectors, whilst the GNC unit provides the own aircraft position and speed. At last, the decision making algorithm are reference signals to the autopilot, in terms of demanded speed module, slope angle and track angle.

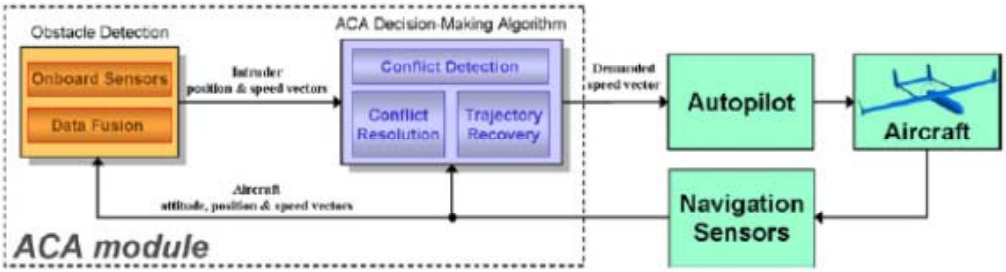

Figure 2.17 ACA system functional architecture within the closed-loop control system

2.2 DS&A System

2.2.1 SENSOR FUSION ARCHITECTURE

The logical architecture of the complete sensor fusion algorithm for flying obstacles detection and tracking is outlined in figure 2.4. and described in detail in ref. 33.

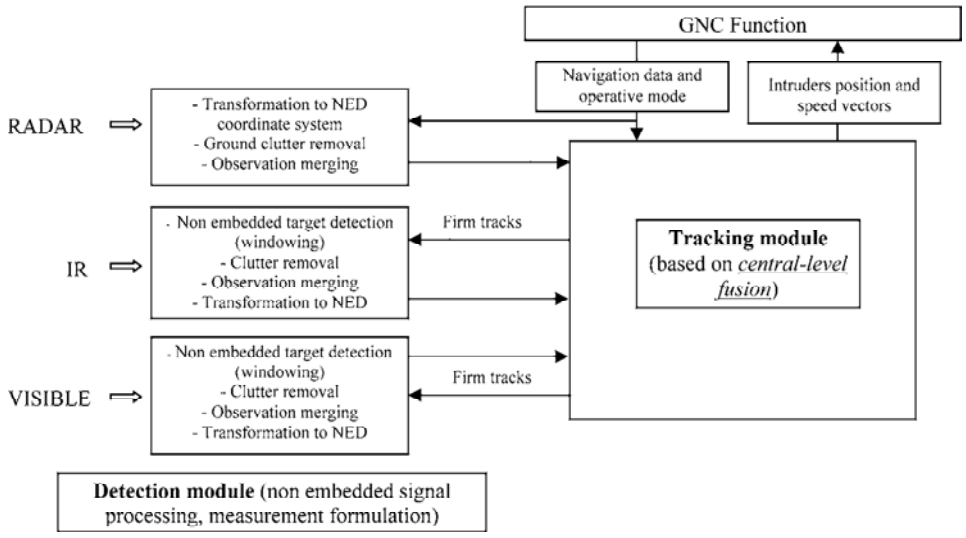

Figure 2.18 Logical architecture of obstacle detection and tracking system

The multi-sensor tracking algorithm is a key element of the DS&A system. In fact, the system is completely autonomous, and thus it is mandatory to have reliable estimates not only of intruder's positions, but also of its motion, as the latter information is needed by the collision avoidance logic to decide whether or not it is necessary to perform an evasive maneuver.

However, the extended Kalman filter (EKF) has been selected as filter of EO and radar data fusion because it resulted the best compromise between accuracy and reliability at very short range, during simplified quasi-collision scenarios ,and it allows for simple track update also with angular measures only (EO sensors). Thus, the Kalman filter output is the GNC function input, and it is characterized by nine components, which are the obstacle coordinates in NED (North-East-Down reference frame with origin in the aircraft center of mass) with their first and second time derivatives.

System components communicate at 10 Hz data rate, which is consistent with the obstacle detection requirements illustrated in a previous section. Moreover, navigation data are used by the algorithm at the same frequency so that UAV dynamics is properly followed during tracking phase without an excessive computational load.

As mentioned earlier, tracking algorithm operates in NED reference frame. This refers not only to the filtering/prediction phase but also to gating and track/measurement correlation. Sensor measurements (both radar and EO) must be converted to NED before being used; therefore they are corrupted by the error in the attitude angles evaluation. As a consequence, tracking performance is closely correlated to the navigation system, and measurement covariance matrix in the Kalman filter must be corrected to account for this additional noise to keep its consistency.

It is worth noting that performing tracking directly in the Body Reference Frame (BRF) with origin in the aircraft center of mass and axes along longitudinal, lateral and vertical aircraft axes, attitude angles' errors are avoided but acceleration and angular velocity measurements (with their errors) must be used in any case. Moreover, the relative

motion in the BRF includes attitude dynamics, unlike its projection in NED, which makes it more difficult to track.

At last, the reader can observe from figure 2.4 that "central-level fusion" for the tracking module is mentioned. It regards the sensor data, which are organized on the basis of a hierarchical structure. In particular, radar is the main sensor, whilst EO system plays a secondary role, auxiliary to radar. However, when radar detects a possible intruder (firm track), it sends its position, in terms of range, azimuth and elevation, to the EO system by means of the RTT-CPU. Thus, the latter performs the second intruder detection and, if it is again positive, the new estimate is sent back to the RTT-CPU, which provides the data fusion and intruder tracking. Therefore, EO cameras do not operate if not solicited by radar question; on the other hand, their outputs provide the increasing of the overall DS&A system for the intruder detection and tracking, in terms of accuracy and data rate.

2.2.2 HARDWARE ARCHITECTURE

The selected radar for autonomous collision avoidance is the AI-130™ OASys™ (Obstacle Awareness System) model produced by Amphitech™. It is a pulsed radar operating with a carrier at 35 GHz and it has been already used for UAV anti-collision flight test by the following centers: 1) NASA in the project ERAST by means of the Proteus aircraft [20]; 2) Northrop Grumman in the DS&AFT project that was sponsored by Air Force Research Labs [29]; 3) German Aerospace Research Centre (DLR) with the experimental Fokker aircraft named ATTAS [34]. The selected frequency provides a good compromise between antenna dimensions, angular accuracy and sensitivity to rain and fog. In the assigned hierarchical sensors architecture, radar is the main sensor, as already stated before. That role depends on its capability of working all-time all-weather and of providing a direct range-to-obstacle measure. It has been

installed on the top of the aircraft behind the wing, central position (figure 2.5).

(a)

(b)

Figure 2.19 (a) Sensors system set on the top of FLARE wing; (b) Zoom of Radar and EO cameras

EO sensors provide auxiliary function to radar, in order to increase accuracy and data rate. They are two visible and two thermal Infrared (IR) cameras located parallel to the aircraft, longitudinal axis to capture simultaneous panchromatic and color high resolution images of the same region. Basically, panchromatic camera outputs provide information of obstacle position, therefore they are processed

for data fusion; whilst, color camera data are devoted to the obstacle identification. Sensors are two Marlin™ cameras produced by Allied Vision Technologies™. Their field of view (FOV) is 49.8° x 38.9°, and they work at the maximum resolution of 1280 x 960 pixels.

The IR cameras are two FLIR™ thermal cameras with a maximum resolution of 320 x 240 pixels and 24° x 18° of FOV. Due their limited angular aperture, they are pointed slightly eccentric to get an azimuth FOV comparable to the visible cameras'.

The obstacle detection and tracking functions are provided by two different processing units, already defined: the RTT-CPU and the IP-CPU. The first one is based on a deterministic Operative System (OS) and it is directly connected to the radar via Ethernet link, through the TCP/IP protocol. It runs the tracking algorithm and performs data exchange with the GNC system, by the CAN bus. The second computer is connected to EO sensors via a Firewire link. It based on a conventional OS and it is dedicated to visible and IR images processing to increase the accuracy of intruder position estimated by radar. Thus, each time radar performs the target detection in the entire FOV, its output is sent to EO sensors which process a part of the whole images; indeed they consider a search window centered on the predicted obstacle position. Moreover only firm tracks are sent to IP-CPU and elaborated by cameras, in order to reduce false alarms.

Additionally, the two processing units communicate by an Ethernet link, on the basis of the UDP protocol. If tracks are generated, they are transmitted from the RTT-CPU to the IP-CPU. Subsequently, the more accurate target position estimates are back sent from the IP-CPU to the RTT-CPU. Their hardware separation allows to reduce the computational load of both computers and to have an improvement of the overall system performance.

The following table synthesizes the exchanged data characteristics between RTT-CPU and IP-CPU, while figures 2.6 and 2.7 show the ODID system installation onboard FLARE and its hardware architecture, respectively.

Table 2.3 Data exchanged between RTT-CPU and IP-CPU

From RTT-CPU to IP-CPU	Predicted range, azimuth (BRF) and elevation (BRF) for firm tracks
From IP-CPU to RTT-CPU	Azimuth (BRF) and elevation (BRF) estimated by the EO sensors, computational time
Data rate	2-10 Hz
Maximum latency	5 ms

Figure 2.20 ODID onboard FLARE

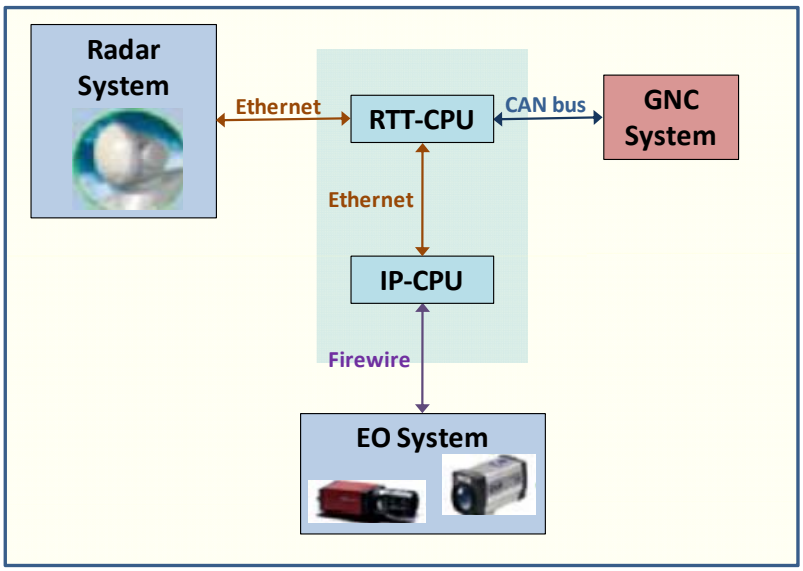

Figure 2.21 ODID hardware architecture

Chapter 3

DETAILS OF EO UNITS

EO system installed onboard FLARE platform is characterized by four cameras: two visible and two IR. Resolution and FOV details have been already presented in the previous section. However, hereinafter we provide more EO sensors details, described by their data sheet, we will describe the process of their calibration onboard the aircraft, with respect to the radar and AHRS systems, and, finally, we will focus more deeply on the image processing algorithm requirements, in particular for the panchromatic camera.

3.1. Camera Data Sheet

Visible cameras are from the same production, one color and one panchromatic. Figure 3.2 is the technical sheet either for the black and white (b/w) model (MARLIN F-145B2) or for the color (MARLIN F-145C2). They are from ALLIED VISION TECHNOLOGIES GMBH [39].

(a) (b)

Figure 3.22 (a) Visible camera lateral view; (b) visible camera backward view

	MARLIN F-145B2 (b/w)	MARLIN F-145C2 (color)
Image Device	1/2 " (Diag 8 mm) type progressive scan SONY IT CCD	
Effective Picture Elements	1392 (H) x 1040 (V): Raw8	1392 (H) x 1040 (V): Raw8; 1392 (H) x 1038 (V) : YUV
Picture Size	1280 x 960 pixel (Format_2); supporting all smaller fixed formats; up to 1392 x 1040 (Format_7 Mode_0)	
Cell Size	4,65 µm x 4,65 µm	
Resolution Depth	8 Bit / 10 Bit (b/w only)	
Lens Mount	C-Mount	
Digital Interface	IEEE 1394; DCAM V1.30	
Transfer Rate	100, 200, 400 Mb/s	
Frame Rates	up to 10 Hz in Format_7	
Gain Control	Manual: 0-24 dB; Auto Gain	Manual: 0-24 dB; Auto Gain
Shutter Speed	11µs...67s; Auto Shutter; Level Mode 00	
External Trigger Shutter	Trigger_Mode_0, Trigger_Mode_1, Advanced feature: Trigger_Mode_15 (bulk); image transfer by command; Trigger delay	
Smart Features	Real time shading correction; built in FIFO Memory up to 3 frames; one user programmable Look Up Table; 2 configurable inputs, 2 configurable outputs; Delayed Image Transfer; sequencing; image mirror (L-R / R-L); serial port (IIDC v. 1.31)	
Power Requirements	DC 8V – 36V via IEEE 1394 cable	
Power Consumption	Less than 3 Watt (@ 12V DC)	
Dimensions	58 mm x 44 mm x 29 mm (L x W x H); w/o tripod and lens	
Mass	<120 gr (without lens)	
Operating Temperature	+5 - 45 ° Celsius	
Storage Temperature	-10 – 60 ° Celsius	
Regulations	EN 55022, EN61000, EN 55024, FCC Class A; DIN ISO 9022	
Options	Removable IR-Cut-Filter; API (FirePackage); TWAIN+WDM (Direct FirePackage); Linux (Fire4Linux)	

Figure 3.23 Visible Cameras data sheet

IR system is composed by two cameras of FLIR production, whose technical information are synthesized in the following.

(a)

(b)

Figure 3.24 (a) IR camera frontal view; (b) IR camera backward view

IMAGING PERFORMANCE	
Field of view / min focus distance	24°x18° /0.3 m (with 35 mm lens)
Spatial resolution (IFOV)	1.3 mrad
Thermal sensitivity	0.08°C at 30°C
Focusing	Built-in focus motor. Manual or automatic focus
Detector type	Focal Plane Array (FPA), uncooled microbolometer (320 x 240 pixels)
Spectral range	7.5 to 13 µm
Image frequency	50/60 Hz
Viewing temperature range	-40°C to +500°C (-40°F to +932°F), in 2 ranges Optional: Up to +1500°C (2732°F) or +2000°C (3632°F)
IMAGE PRESENTATION	
Image output	RS170 EIA/NTSC or CCIR/PAL composite video IEEE-1394 FireWire output (optional) RJ-45 Ethernet output (optional)
LENSES (OPTIONAL)	
Field of view / min focus distance	7° x 5.3°/4 m (with 122 mm lens) 12° x 9°/1.2 m (with 71 mm lens) 45° x 34°/0.1 m (with 18 mm lens) 80° x 60°/0.1 m (with 9 mm lens) 200 µm close-up (64 mm x 48 mm/150 mm) 100 µm close-up (34 mm x 25 mm/80 mm) 50 µm close-up (15 mm x 11 mm/19 mm) 18 µm close-up (6 mm x 4 mm/7 mm)
Lens identification	Automatic
POWER SOURCE	
AC operation	AC adapter 110/220 V AC, 50/60 Hz
Voltage	10/30 V nominal, < 6 W
ENVIRONMENTAL SPECIFICATIONS	
Operating temperature range	-15°C to +55°C (+5°F to +122°F)
Storage temperature range	-40°C to +70°C (-40°F to +158°F)
Humidity	Operating and storage 10% to 95%, non condensing
Encapsulation	IP 40 (determined by connector type)
Shock	Operational: 25G, IEC 68-2-29
Vibration	Operational: 2G, IEC 68-2-6
PHYSICAL CHARACTERISTICS	
Weight	1.4 kg (3.1 lbs)
Size	207 mm x 92 mm x 109 mm (8.2" x 3.6" x 4.3")
Tripod Mounting	1/4" - 20
INTERFACES	
Digital image output and camera control	6-pin FireWire (IEEE-1394) connector handling iso-chronous 16-bit digital image data and asynchronous control data or standard RJ-45 Ethernet connector handling image data (RTP) and control data (TCP/IP)
BNC	Composite video (NTSC/PAL)
6-pin screw terminal (upper)	Digital I/O: 3 Output - 1 Input 1 Input/Output selectable. User configurable*
6-pin screw terminal (lower)	Analog I/O: 2 Output - 1 Input User configurable* - see user configuration table

Figure 3.25 IR camera data sheet

3.2. Cameras Calibration

3.2.1 INTRINSIC CALIBRATION

Intrinsic calibration has been performed for visible cameras by imaging a sample pattern from different points of view, in order to evaluate the effects of distortion of lens on the acquired images. That technique is based on a Matlab™ Toolbox accurately described in ref. 45.

As regards the IR cameras, optical distortions have been considered negligible because of their little FOV, so that a linear law of association between target and pixel is applicable.

However, the intrinsic calibration of visible cameras has allowed us to estimate their optical parameters, such as the focal length, the principal point and the distortion coefficients, which we present synthetically hereinafter.

Table 3.4 Panchromatic camera Intrinsic Parameters

Focal length = [1434.115; 1436.389] pixels; **Principal point** = [643.563; 473.611] pixels; **Skew Coefficient** = 0.000 pixels; **Distortion coefficients** = [-0.240; 0.201; 0.001; 0.002;0.000]pixels;

Table 3.5 Visible camera Intrinsic Parameters

Focal length = [1448.752; 1451.470] pixels; **Principal point** = [644.576; 483.668] pixels; **Skew Coefficient** = 0.000 pixels; **Distortion coefficients** = [-0.236; 0.206; 0.001; 0.001;0.000]pixels;

The reader can observe that a 4^{th} order "plump bob" model has been assumed to describe the optical distortions of lens for both visible cameras. However, for standard field of views (non wide-angle cameras), it is often not necessary (and not recommended) to push the radial component of distortion model beyond the 4th order. In addition, the tangential component have been discarded (justified by the fact that most lenses currently manufactured do not have imperfection in centering). The 4th order symmetric radial distortion with no tangential component is actually the distortion model used by Zhang [46].

Finally, the following figure represents the estimated distortion model of the panchromatic camera.

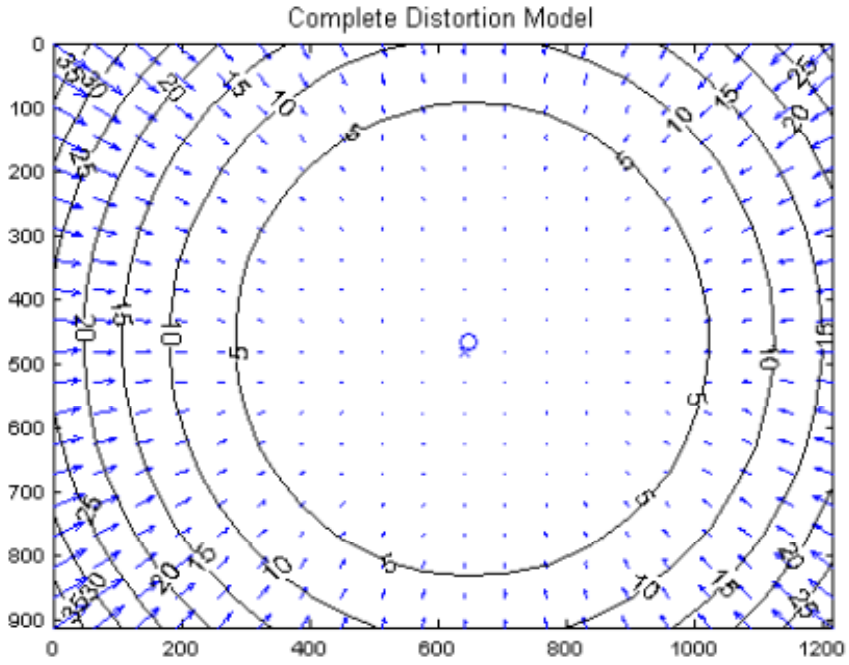

Figura 3.26 Panchromatic camera Optical Distotion Model

3.2.2 EXTRINSIC CALIBRATION

EO sensors have been accurately aligned onboard the FLARE aircraft, on the basis of a assessed procedure, described in detail in ref. 40. In particular, that calibration technique is very valid to align EO cameras in strapdown and forward looking installation; indeed, the technical term used to identify that operation of calibration is "boresighting" [41].

However, the adopted technique has allowed us to align all the EO sensors set simultaneously, taking into account the attitude measurements provided by the onboard AHRS and the Carrier phase Differential GPS (CDGPS) measurements. Thus, the aim of the considered boresighting method is to determine the rotation matrices between sensors' reference frame and aircraft Body Reference Frame (BRF) (X-nose, Y-right wing, Z-down), basing on the least square technique (q-method), which estimates the transformation matrix for

each camera by a series of vector observations of the same in two reference frames [42].

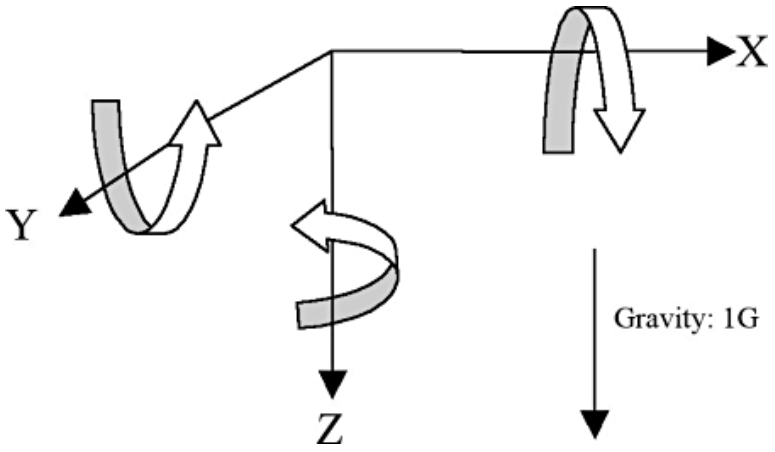

Figure 3.27 BRF convention

Hereinafter, GPS and AHRS systems details are illustrated. However, the central unit is the AHRS400CC™ manufactured by Crossbow™. It is a high performance solid-state attitude and heading reference system. In static mode, by averaging sensors output for some seconds (data rate is 100 Hz), it is possible to reach an accuracy of the order of 0.1°.

The ground GPS antenna is the LegAnt™ manufactured by Topcon™, whereas other two GPS antennas are located on the aircraft wings. The measurement technique is the Real Time Kinematic (RTK) carrier-phase differential mode which is a process where GPS signal corrections are transmitted in real time from a reference receiver at a known location to another receiver. The use of an RTK capable GPS system can compensate atmospheric delay, orbital errors and other variables in GPS geometry, increasing positioning accuracy. Using the code phase of GPS signals, as well as the carrier phase, which delivers the most accurate GPS information, RTK provides differential corrections to produce the most precise GPS positioning.

Figure 3.28 AHRS and GPS antenna installed onboard FLARE

3.2.3 THE CALIBRATION PROCEDURE

In order to determine a target position as in the sensors' reference frame as in the BRF, more operations have to be performed at the same time: at least two images of the target have to be acquired by all the cameras, target position has to be provided by the CDGPS, aircraft attitude is measured by AHRS. At the end of the acquisitions, cameras' positions must be measured by CDGPS with the same level of accuracy. For the sake of clarification, in this section BRF will be considered as a synonym of AHRS-defined reference frame.

Figure 3.8 shows part of the hardware set-up during a calibration session.

Figure 3.29 Calibration session: target and cameras' relative position

From a statistical point of view, a large number N of target positions allows the pointing estimation accuracy to be improved of a $N^{-0.5}$ factor. Therefore fewer measurements, but very accurate, produce a better pointing accuracy.

In order to establish how many targets positions are to be measured, and at what distance the target must be placed, both CDGPS accuracy and sensors IFOV must be taken into account. In fact, in theory the best solution would be to place the target as far as possible from the sensor, so that the GPS error falls below single pixel angular dimensions. However, this makes target positioning harder to realize. In fact, in order to have a globally accurate alignment, the test points should be selected uniformly in the cameras field of view. In the considered case, the relevant accuracies are shown in table 3.3.

Table 3.6 Sensors accuracies

GPS accuracy in carrier-phase mode	3 mm + 1 ppm
VIS cameras Instantaneous Field Of View (IFOV)	0.041°
IR cameras IFOV	0.074°

By a simple geometric relationship, it is possible to determine at what distance the GPS precision equals the

linear dimension which corresponds to the cameras IFOV. Some numerical data for the considered case are shown in table 3.4.

Table 3.7 Linear dimensions of FOV and IFOV for several distances

Distance (m)	2	4	5	10	20
Width FOV VIS	1.805	3.610	4.513	9.025	18.050
Height FOV VIS	1.361	2.722	3.402	6.805	13.610
Width FOV IR	0.850	1.700	2.124	4.249	8.498
Height FOV IR	0.633	1.266	1.583	3.166	6.332
Length IFOV VIS	0.001	0.003	0.004	0.007	0.014
Length IFOV IR	0.003	0.005	0.006	0.013	0.026

From table 3.4, the reader can easily conclude that the procedure can be implemented by locating the target at a distance of about 4 meters from the focal plane of the sensors and moving it in a rectangle of about 4 m X 3 m. Thus, that was the distance selected in the performed calibration tests.

The basic assumption of q-method is that the main component of the error of the single observations is random, thus it is supposed that the camera is perfectly calibrated. This means that optical distortion is neglected either in the IR or in the visible cases. It can be stated that this assumption can be considered consistent with the scopes of this application, also because of the narrow field of view of the cameras. On the other hand, the validity of this assumption has been verified by several tests and reported in ref. 40.

During tests, EO sensors acquire images simultaneously, and for each of them target centre pixel is easily detectable, then its coordinates can be translated into angular information by exploiting the camera intrinsic parameters.

Thus, given the target and the camera position in the Earth-Centered Earth-Fixed (ECEF) reference frame, it is possible to evaluate the target position in the North East Down (NED) reference frame with origin in the camera, trough an exact transformation [43]. Subsequently, the target position r_{iNED} can be transformed in the BRF on the basis of the attitude AHRS measurements, by the following relation:

$$r_{iBRF} = M_{321}(\gamma, \beta, \alpha)\ r_{iNED} \tag{3.1}$$

Where γ, β, α are, respectively, the heading, pitch and roll angles, and the matrix M_{321} is obtained as follows:

$$M_{321} = \begin{bmatrix} \cos\beta\ cos\gamma & cos\beta\ sin\gamma & -sin\beta \\ -cos\alpha\ sin\gamma + sin\alpha\ sin\beta\ cos\gamma & cos\alpha\ cos\gamma + sin\alpha\ sin\beta\ sin\gamma & sin\alpha\ cos\beta \\ sin\alpha\ sin\gamma + cos\alpha\ sin\beta\ cos\gamma & -sin\alpha\ cos\gamma + cos\alpha\ sin\beta\ sin\gamma & cos\alpha\ cos\beta \end{bmatrix} \tag{3.3}$$

It is worth noticing that AHRS systems measure heading angle with respect to the magnetic North, while the transformation from ECEF to NED refers to geographic North. Thus, AHRS heading measurements must be summed to magnetic declination, in order to not introduce a systematic error in alignment.

Furthermore, the cosine directors of the line-of-sight to the target, characteristic of the considered camera and the i-th image, are calculated by dividing the r_{iBRF} to its module. However, let us call $\hat{r}_{iBRF}$ and $\hat{r}_{iSENS}$ the computed unit vector and the unit vector of the target direction in the Camera Reference Frame (CRF), as extracted by the i-th image. Assuming that CRF axis have the same convention of the BRF axes, it now possible to define the loss function:

$$J(M_{CAM}) = \sum_{1=1}^{n} w_i \left| \hat{r}_{iSENS} - M_{CAM}\ \hat{r}_{iBRF} \right|^2 \tag{3.2}$$

Where n is the number of collected images/positions, w_i is the weight of the i-th measurement (in this case, all of

them have the same value) and M_{CAM} is the attitude matrix of the considered camera with respect to the aircraft. Thus, we select M_{CAM} as the matrix which minimizes J; so, it can be computed by means of the q-method algorithm which calculates attitude in terms of optimal least-square quaternion [42].

At last, for the sake of clarification, the following figure illustrates the CRF applied at an acquired panchromatic image where the target is present. It is based on the classical pinhole model [44], where the image is in front of the projection centre, and demonstrates that there is the same axes convention of the BRF.

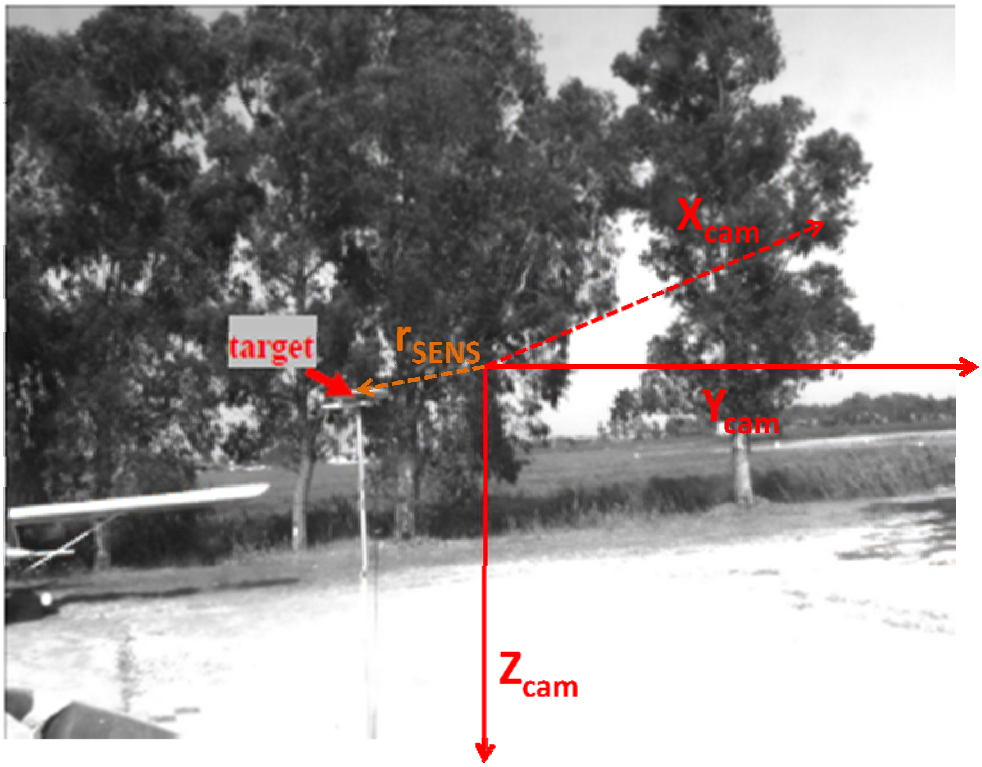

Figure 3.30 CRF applied at a panchromatic image

3.3. Processing

As already stated before, EO system provides an auxiliary role to radar, in order to increase the accuracy and data rate of its measurements. However, IP-CPU works subsequently to RTT-CPU, as soon as a detected target becomes firm track (an obstacle is defined "firm track" when radar associates its presence to, at least, three on five detected obstacles).

In particular, different auxiliary functions are assigned to the EO system: panchromatic camera is used for obstacle detection and its output is fused with radar estimate in the Kalman filter [33]; the color camera aims at obstacle identification; IR cameras perform the obstacle detection in dark luminosity conditions, in order to replace panchromatic camera where it is not able to work.

At the moment, only processing by panchromatic camera has been analyzed and tested, because it plays the most important auxiliary role to radar in order to realize a reliable DS&A system, which can substitute human's eyes.

In particular, the hierarchical obstacle detection process for the panchromatic camera is structured in the following way: intruder range, azimuth and elevation as estimated by the radar-based tracking algorithm are sent from RTT-CPU to IP-CPU and constitute the input data to the image processing algorithm, which converts them from the aircraft Body Reference Frame (BRF) to the Camera Reference Frame (CRF) (based on the camera alignment matrices estimated by the procedure explained before [40]), and compares them to the camera FOV. If the intruder position is within the FOV, the image processing routine starts and the panchromatic camera analyzes only the image portion enclosed in the search window

centered on the intruder position detected by radar, with width and height depending on intruder range. In this way, the object detection algorithm can generate an accurate estimate of intruder angular position in the CRF. In case of detection, this estimate is converted back to the BRF and transmitted to the RTT-CPU. Since only a portion of the whole image is analyzed, the object detection algorithm runs very fast thus minimizing the latency in providing measurements to the multi-sensor tracking filter.

Figure 3.10 is a clarifying example of the main steps regarding the EO obstacle detection SW by panchromatic camera.

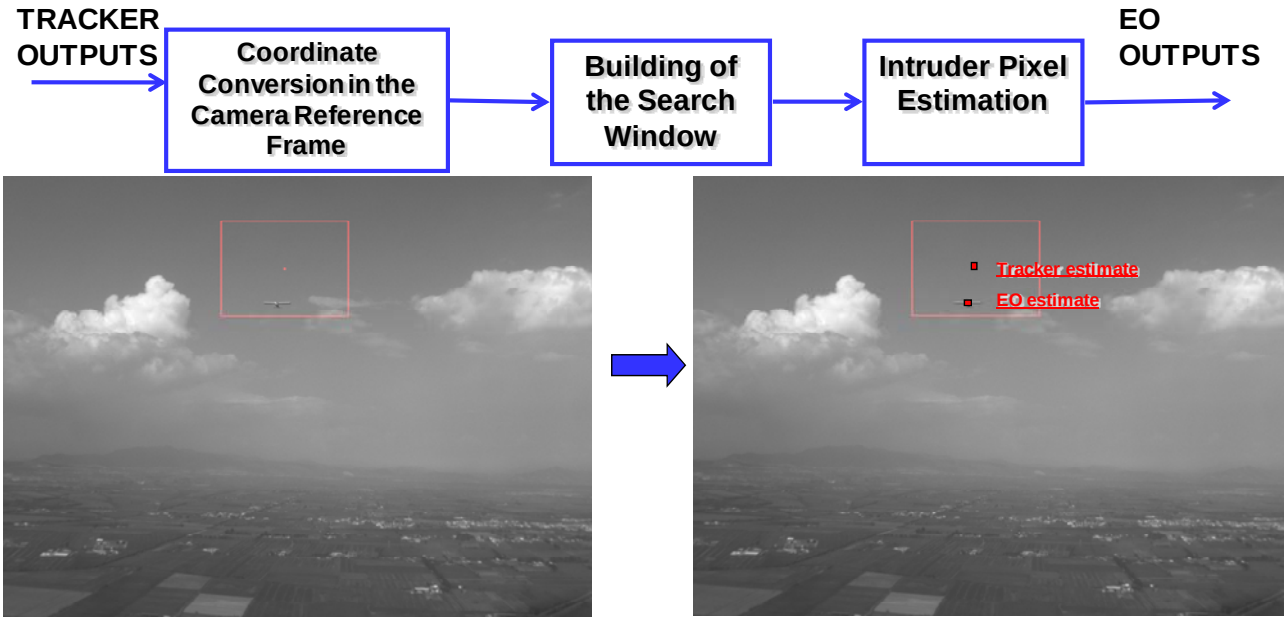

Figure 3.31 Panchromatic camera image processing algorithm main steps

That is the general panchromatic camera SW structure. Next chapters will be concerned, more in detail, on its performance, the chosen image processing technique, the reasons of that choice and how it fulfills the DS&A requirements.

Chapter 4

IMAGE PROCESSING ALGORITHMS

EO system engineering started development at various locations throughout the world just prior to World War II. Primarily, it was relegated to laboratory interest, and, subsequently, it found wide applicability in the military field. However, optics and sensors have continued to evolve, and, nowadays they have had the starring growth in capability of automatic target cuers (ATCs) and recognizers (ATRs) for automatic multisensor systems. Indeed, when we talk of EO object detection system, the prime decision maker is still the human being; therefore, many research studies have been carrying out all over the world with the aim of realizing fully automatic ATC and ATR systems, which could be able to substitute completely the human's eyes.

Thus, when evaluating EO system for target detection, it is necessary to talk in terms of probabilities of detection, recognition, classification, and identification, together with the modalities of performing such analyses, and the choice of the appropriate method. Indeed, such probabilities depend on many external and internal to EO system factors, such as the contrast between target and background, the atmosphere and the display.

This chapter aims at presenting some of the most common image processing techniques, applied at several international

research programs in the automatic target detection field. However, we will describe their main theoretical aspects, and we will present some examples of application; moreover, we will compare them, on the basis of their performance limits and advantages.

4.1 BINARIZATION

Binarization is a detection technique which aims at segmenting an image on the basis of a threshold fixed on its histogram of luminosity. Consequently, image is distinguished in two different classes, characterized by luminosity values above and under the set threshold. However that method is also named image segmentation with thresholding and, due to the rapidity of calculus, its suitable for real-time system [47,48,49,50]. Thus, if the threshold is fixed during all the image processing execution, the technique is defined static thresholding, whose algorithm is expressed as follows:

$$\forall x,y:\ S(x,y) = \begin{cases} 1 & \text{if} \quad I(x,y) \geq T \\ 0 & \text{if} \quad I(x,y) < T \end{cases} \tag{4.1}$$

where I(x,y) is the image function, T is the set threshold, (x,y) are the pixel coordinates in the image plane, and S(x,y) is the output binarized image.

Figure 4.1 represents an image whose object can be easily separated from the background, applying a threshold between 100 and 200, as the reader can evaluate from its histogram of luminosity.

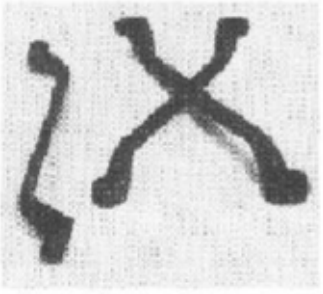

Figure 4.32 Image of Analysis

Figure 4.33 Binarized Image

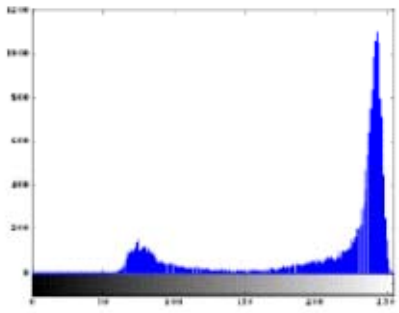

Figure 4.34 Image Histogram of Luminosity

Static thresholding has a limited field of application, which regards above all the processes of automatic industrialization [50], where usually image background luminosity is constant and of strong intensity, so that it is easily distinguishable from targets.

More general cases of application consider variable thresholds, depending on the image spectral analysis. Indeed the technique is defined "dynamic thresholding" [49], which consists in selecting the most suitable threshold for the instantaneous acquired image, whose background differs rapidly during the time of experimentation. Although its merits, that algorithm has not very success in real-time system, due to its heavy computational load.

As regards target detection in the aerospace field, binarization is widely considered in automatic UAV take-off and landing projects [51]. However, ground images are processes by the simple thresholding technique, which provides the black and white image, and subsequently algorithm works to determine ground target centroid in the overall image.

In particular, the x and y centroids with respect to the image plane are calculated as:

$$x = \frac{\sum_{i=1}^{N} x_i}{N}$$

$$y = \frac{\sum_{i=1}^{N} y_i}{N} \qquad (4.2)$$

Where N is the number of pixels which characterize the ground target, x_i and y_i are their coordinates in the image plane.

Finally, ground target position in the image plane is converted to the CRF by coordinate's transformation which is based on EO camera intrinsic parameters and UAV altitude [45]. The following figure illustrates a generic case of relative positioning between image plane and CRF.

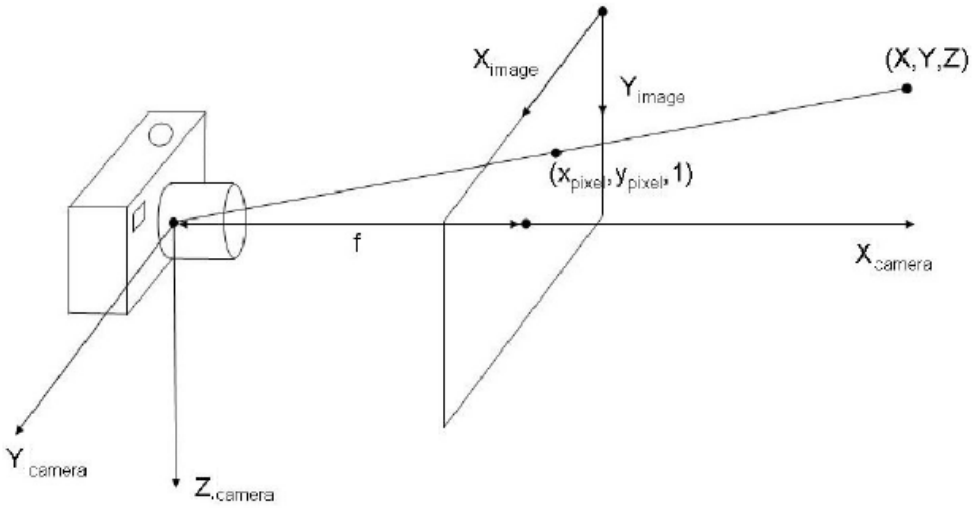

Figure 4.35 Image Plane with respect to CRF

At last, it's worth mentioning the partial thresholding, which is often applied in order to reduce the computational time and, indeed, it consists in binarizing only on a portion of the overall image [52]. An example of application is illustrated in the following figures, where it's a priori known that intruder aircrafts are above the horizon line, therefore image is segmented and only the upper half part is processed.

Figure 4.36 Overall Panchromatic Image

Figure 4.37 Portion of image processed by thresholding

4.2 EDGE DETECTION

Edge detection is a very important area in the field of Computer Vision [53-59]. Edges define the boundaries between regions in an image, which helps with segmentation and object recognition.

In particular, the edge detection technique main goals are:

- Producing a line drawing of a scene from an image of that scene;
- Extraction of important features from the edges of an image(e.g., corners, lines, curves);
- Using of these features by higher-level computer vision algorithms (e.g., recognition).

Generally, edges are caused by significant local changes of intensity in an image; however, several physical events cause intensity changes: geometric and non-geometric events.

The first ones are object boundary (discontinuity in depth and/or surface color and texture) and surface boundary (discontinuity in surface orientation and/or surface color and texture); whilst, non-geometric events are specularity (direct reflection of light, such as a mirror), shadows (from other objects or from the same object) and inter-reflections.

Moreover image edges are described by four parameters, whose two are depicted in figure 4.7.

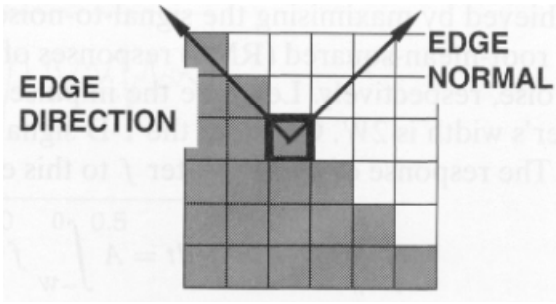

Figure 4.38 Image Edge Representation

In particular, the edge normal is the unit vector in the direction of maximum intensity change; the edge direction is the unit vector to perpendicular to the edge normal; the edge position or center is the image position at which the edge is located; and the edge strength is related to the local image contrast along the normal.

In addition, several types of edges can be defined:

- Step edge: the image intensity abruptly changes from one value to one side of the discontinuity to a different value on the opposite side;
- Ramp edge: a step edge where the intensity change is not instantaneous but occur over a finite distance;
- Ridge edge: the image intensity abruptly changes value but then returns to the starting value within some short distance (generated usually by lines);
- Roof edge: a ridge edge where the intensity change is not instantaneous but occur over a finite distance (generated usually by the intersection of surfaces).

For clarification, hereinafter we present some graphical illustration of those edges in terms of their intensities changes.

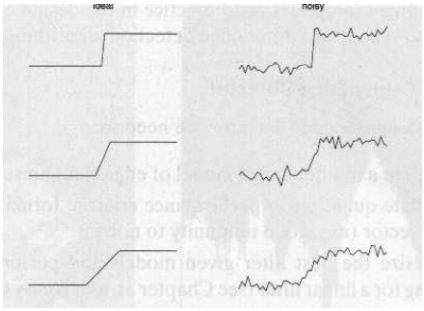

(a)

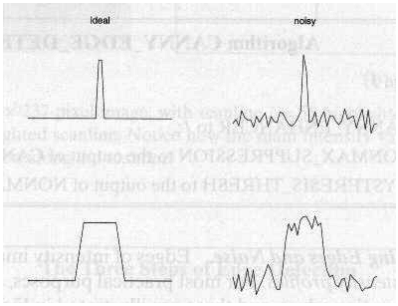

(b)

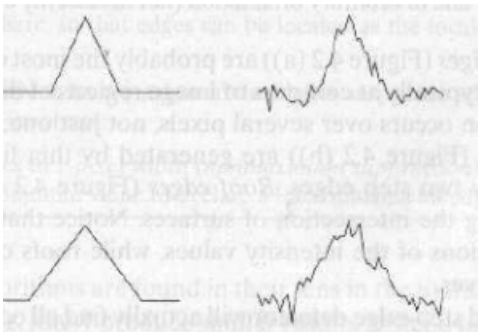

(c)

Figure 4.39 (a) Step and Ramp Edge in ideal and real cases; (b) Ramp edge in ideal and real cases; (c) Roof edge in ideal and real cases

There more edge detection methods, which are based on different theoretical principles of detection of intensities changes, which characterize the image in analysis. They can be distinguished in "edge detection using derivatives" and "edge detection using gradient". Anyway, both groups of methods are based on four main steps of processing:

- Smoothing: suppress as much noise as possible, without destroying the true edges.
- Enhancement: apply a filter to enhance the quality of the edges in the image(sharpening).
- Detection: determine which edge pixels should be discarded as noise and which should be retained (usually, thresholding provides the criterion used for detection).

- Localization: determine the exact location of an edge (sub-pixel resolution might be required for some applications, that is, estimate the location of an edge to better than the spacing between pixels). Edge thinning and linking are usually required in this step.

The description of the first group of edge detection techniques is out from our interest, because it deals with very heavy methods, not suitable for real-time systems as well as for automatic target recognition systems.

Thus, we will be focused on the edge detection methods, based on the using of gradient, and which find a wide field of application in the real-time vision-based navigation [55-59].

4.3.1 Edge Detection Using Gradients

From mathematics, let us call gradient of a function f(x,y), the vector whose magnitude and direction are:

$$magn(\nabla f) = \sqrt{(\frac{\partial f}{\partial x})^2 + (\frac{\partial f}{\partial y})^2} \quad = \quad \sqrt{M_x^2 + M_y^2} \tag{4.3}$$

$$dir(\nabla f) = tan^{-1}(\frac{M_y}{M_x}) \tag{4.4}$$

For computational time reasons, the magnitude of gradient is usually approximated by the sum of its components:

$$magn(\nabla f) \approx |M_x| + |M_y| \tag{4.5}$$

While, the partial derivatives are simplified by finite differences:

$$\frac{\partial f}{\partial x} = f(x+1,y) - f(x,y), \ (h_x = 1) \tag{4.6}$$

$$\frac{\partial f}{\partial y} = f(x,y+1) - f(x,y), \ (h_y = 1) \tag{4.7}$$

Thus, using pixel-coordinate notation, expressions (4.6) and (4.7) become:

$$\frac{\partial f}{\partial x} = f(i,j+1) - f(i,j) \tag{4.8}$$

$$\frac{\partial f}{\partial y} = f(i,j) - f(i+1,j) \tag{4.9}$$

where i and j correspond to the Y_{image} and X_{image} of figure 4.4, respectively.

From those theoretical principles, more edge detectors based on gradient have been developed; basically, they differ for the considered mask of image derivation with respect to a reference pixel (i,j). Thus, we present hereinafter the main edge detectors and their filters of derivation.

- The **Roberts** edge detector is characterized by the following masks of derivation:

$$I_x = \begin{bmatrix} 1 & 0 \\ 0 & -1 \end{bmatrix} \qquad I_y = \begin{bmatrix} 0 & -1 \\ 1 & 0 \end{bmatrix} \tag{4.10}$$

  So the magnitude of the gradient applied at the image I in the pixel (i,j) is:

$$magn\,(\nabla I) = f(i,j) - f(i+1,j) + f(i+1,j) - f(i,j+1) \tag{4.11}$$

- The **Prewitt** and **Sobel** edge detectors are based on common expressions of the partial derivatives:

$$M_x = (a_2 + ca_3 + a_4) - (a_0 + ca_7 + a_6) \tag{4.12}$$

$$M_y = (a_6 + ca_5 + a_4) - (a_0 + ca_1 + a_2) \tag{4.13}$$

  Thus, setting c = 1 we get the Prewitt operator:

$$I_x = \begin{bmatrix} -1 & 0 & 1 \\ -1 & 0 & 1 \\ -1 & 0 & 1 \end{bmatrix} \qquad I_y = \begin{bmatrix} -1 & -1 & -1 \\ 0 & 0 & 0 \\ 1 & 1 & 1 \end{bmatrix} \tag{4.14}$$

  Whilst, setting c = 2, we the Sobel operator:

$$I_x = \begin{bmatrix} -1 & 0 & 1 \\ -2 & 0 & 2 \\ -1 & 0 & 1 \end{bmatrix} \qquad I_y = \begin{bmatrix} -1 & -2 & -1 \\ 0 & 0 & 0 \\ 1 & 2 & 1 \end{bmatrix} \tag{4.15}$$

  However, the Sobel edge detector gives more emphasis to pixels closer to the center of the mask.

- The **Canny** edge detector has the peculiarity of considering the Gaussian function G(x,y) to build the masks of filtering; however they have the following expressions:

$$I_x = \frac{\partial}{\partial x}(f * G) = f * \frac{\partial}{\partial x}G = f * G_x \qquad (4.16)$$

$$I_y = \frac{\partial}{\partial y}(f * G) = f * \frac{\partial}{\partial y}G = f * G_y \qquad (4.17)$$

Moreover, after the image derivatives calculus, a thresholding phase is performed, during which a black and white image is generated, applying a reference threshold of binarization on the gradient image.

(a) (b)

Figure 4.40 (a) Reference Image; (b) Processed Image after Image Gradient Calculus and Binarization

Each method is characterized by own detection performance, which can be synthesizes in:

- good detection: minimizing the probability of false positives, caused by noise;
- good localization: edges are as close as possible to real edges;

- single response contrast: the detector must return one point for each one point;
- computational time.

However, the most widely used edge detector in computer vision is the Canny method, because it is able to suppress as much background noise as possible by means of the Gaussian smoother and to provide good performance in the localization and single response contrast; indeed, in real-time application it is not preferable, due to its heavy computational load which increases with the filtering size, frequent choice, applied when more smoothing effects are desired.

Finally, hereinafter we present a reference figure processed by the Sobel and Canny edge detectors. For both, the same threshold of binarization is considered; the reader can observe that the Canny method smoothing effects are more consistent as much as the filtering size increases, so that also the computational load grows up. Thus, Sobel method is the most common solution adopted in real-time applications [57], due to its light computational load, due to the emphasis it gives to the edges points by means of the coefficient 2 of its kernel, and its good smoothing effects which are stronger than Roberts', whose filtering matrix is the littlest.

Figure 4.41 Reference Image

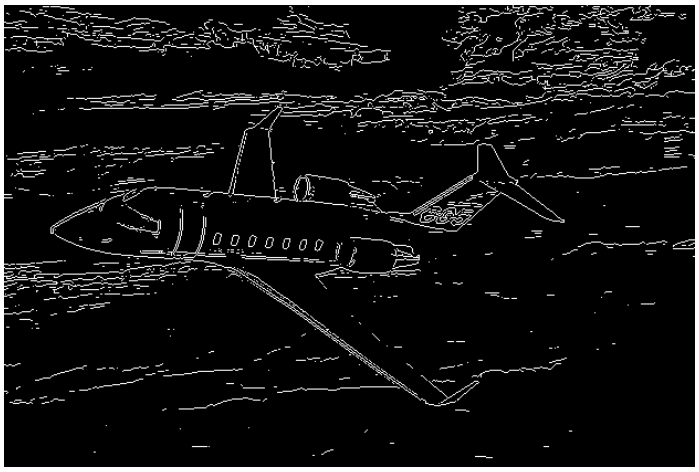

Figure 4.42 Sobel edge Detector

Figure 4.43 Canny Edge Detector with 3x3 Gauss Filter

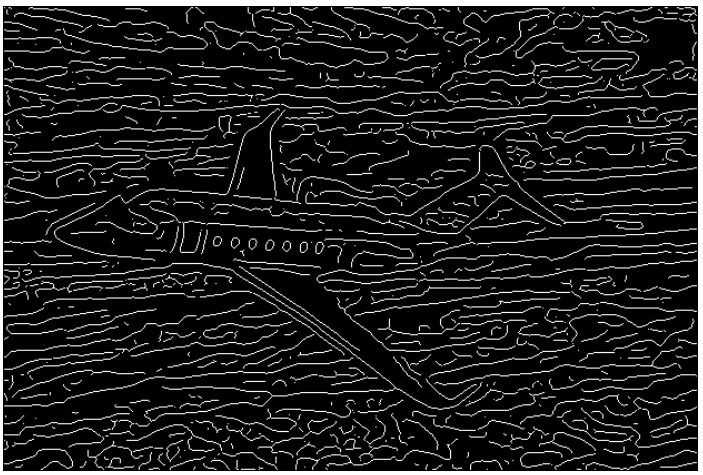

Figure 4.44 Canny Edge Detector with 5x5 Gauss Filter

4.2.2. Edge Detection Application in the Aerospace Field

An example of aerial images, processed by edge detection, is represented by the project carried out by Blue Bear Systems Research and the Cranfield University, which aims at performing automatic land-sea search and surveillance operations on UAV platforms [59]. However, the chosen image processing technique is the edge detection which has presented good performance of identifying salient object of the acquired images.

Some obtained results are presented in the following figures, where detected objects are signed by red rectangles.

(a)

(b)

Figure 4.45 (a) Land image by UAV; (b) Sea image by UAV

Other studies involve edge detection in forward-looking UAV applications, for intruder aircraft platforms detection and tracking [56].

4.3 CORNER DETECTION

Currently, corner detection is widely used in many industrial applications, such as the ones concerning the object identification [60] and tracking in real-time systems [61-63]. However, it is demanding the improvement of this technique in terms of computational load; that effort has been carrying out also by the French Aerospace Research Lab ONERA, in the framework of the ReSSAC project [16], which involves an unmanned helicopter platform, where vision-based navigation and target tracking systems are installed onboard in order to allow the drone to fly fully autonomously in an unknown urban environment. Thus, about the ability of performing autonomous landings at unprepared sites, the terrain characterization is a necessary step for UAVs, when they select autonomously a landing location. However, ONERA ReSSAC helicopter studies the terrain by means of a nadir-mounted camera, which applies a monocular stereovision technique, based on the motion of the UAV. In particular stereovision algorithm roughly works in the following way:

1. Selection of points of interest in the image;
2. Matching of the selected points between two following images;
3. Triangulation and estimation of the relative localization of objects corresponding to these points.

As regards, the first point, the corner detection technique is applied; however, a very fast terrain feature detection algorithm is demanded, and it requires a strong improvement of the classical corner detection techniques: Shi-Tomasi [64] and Harris-Stephens [65].

As follows, a brief description of those corners detection technique and their theoretical principles.

4.3.1 Criterions of Detection of the Points of Interest

Image features, or points of interest are a very broad concept which, generally, indicates the image points with particular characteristics, used to match two or more consecutive images. From the Harris point of view [65], an image feature is a corner, detected by computing on each pixel a saliency degree taking into account the local texture surrounding the considered pixel. Texture is related to local variations of pixel's intensity around the considered point.

In particular, the corner detection criterion is based on a score calculated for each pixel from two eigenvalues of the image, considered as matrix; after that, the searching of score maximum values is implemented; they correspond to the image corners.

The Shi-Tomasi corner detector is based entirely on the Harris corner detector [64]. However, this method differs from the previous one in the pixel score evaluation, which depends only on eigenvalues, in order to determine if a pixel is corner or not.

In detail, we illustrate the equations that characterize the two methods and that provide more clearly their differences.

Let us consider the image array I(x,y), with x and y respectively horizontal and vertical pixel indexes, and we define $I_x(x,y)$ and $I_y(x,y)$ the first order directional differentials, provided by a differential operator, such as Sobel, Prewitt, Roberts etc. [53]. We can build the symmetric autocorrelation matrix S(x,y) in the neighborhood of the pixel (x,y) in the following way:

$$S(x,y) = \sum_{x,y} w(x,y) \begin{bmatrix} I_x^2(x,y) & I_x(x,y)I_y(x,y) \\ I_x(x,y)I_y(x,y) & I_y^2(x,y) \end{bmatrix} \quad (4.18)$$

where w(x,y) is a smoothing function that weighs differently the points of the considered neighborhood; its characteristic function can be square, triangular or Gaussian.

Let us indicate λ_1 and λ_2 the eigenvalues of matrix S(x,y), given by of the second order equation:

$$\lambda^2 - \lambda \times \text{track}(S) + \det(S) = 0 \qquad (4.19)$$

Both Harris and Shi-Tomasi methods are based on pixel scores, depending on eigenvalues.

Indeed, Harris calculates that score as explained hereinafter:

$$C_{\text{Harris}}(x, y) = \det[S(x, y)] - k * \text{track}^2[S(x, y)] \qquad (4.20)$$

where k is an empirical value, usually fixed as 0.06 [66], and det[S(x,y)] and track[S(x,y)] depend on the eigenvalues by the following equation:

$$\det[S(x,y)] = \lambda 1 \quad \lambda 2; \qquad (4.21)$$

$$\text{track}[S(x,y)] = \lambda 1 + \lambda 2 \qquad (4.22)$$

On the other hand, the Shi-Tomasi method evaluates the pixel score on the basis of a more simple relation (4.23):

$$C_{\text{Tomasi}}(x, y) = \min(\lambda_1, \lambda_2) \qquad (4.23)$$

Maximum values of C(x,y) parameter are the image points of interest, as in the Harris as in the Shi-Tomasi cases. Therefore, when the user asks for a selected number of corners, the algorithm lists the C(x,y) values in ascending order, and provides the position of pixels which correspond to the first values of the list, on the basis of the requested number of corners.

4.3.2 Fast Corner Detection Algorithms

Many cases of study have been implemented in order to slight the classical corner detection technique, which requires long times of computation. However, we can mention many international experiences [67-69], as well as the French one [70]. In each case, some geometric figures have been taken as reference and corner detection time of those figures is evaluated. The following image is the test image adopted by ONERA; red crosses are the algorithm outputs. The respective evaluated computation time is 45 ms for Image in Video Graphics Array (VGA) resolution (640x480) and 13 ms for binned VGA images (320x240) [71].

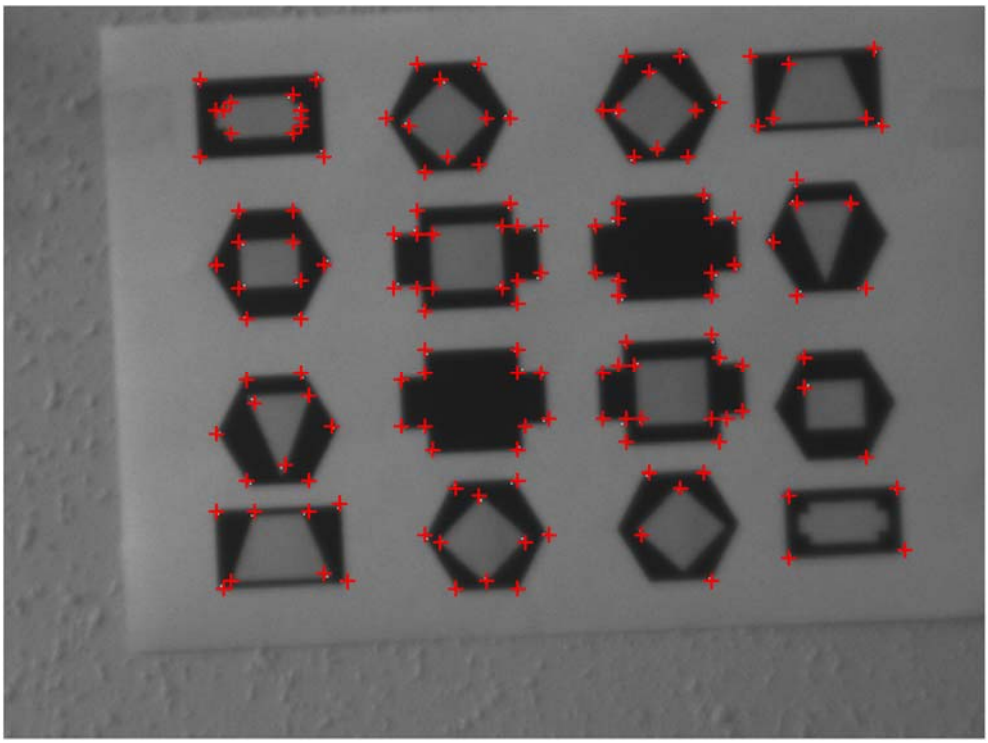

Figure 4.46 Corner Detection Test Image

4.4 CLUSTERING

Clustering is another common technique to detect and isolate objects from background of an analyzed image. However, it consists in detecting one or more clusters in the overall image, each of them representing a characteristic object, and

subsequently the method outputs one object position, on the basis of established criterions of choice.

Several methods can be applied to cluster an image; the most common is based on a thresholding technique which provides more clusters, one for each assigned thresholds range; furthermore, the biggest cluster is chosen as the object of the research, so it is the clustering algorithm output.

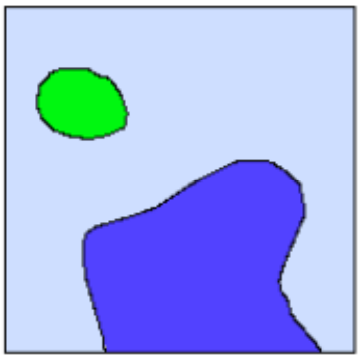

Figure 4.47 Image with two clusters

From literature, that method is often discarded in real-time executions due to its computational load, which is already heavy for images with three clusters [47].

Some studies have been implemented in order to reduce the time of computation, to introduce that method also in automatic surveillance applications. However, the Laboratory of Speech an Image Information Processing of the Northwestern Polytechnical University of China has experimented an online clustering-based passenger counting system, suitable for real-time systems; indeed, results show that the system can process two 320 x 240 video sequences at a frame rate of 25 fps simultaneously and it is quite reliable for different scenarios background [72].

Moreover, similar studies have been carried out by the University of Zaragoza, which has designed a real-time algorithm to detect and classify football players during a

match. Thus, that algorithm is based on the clustering logic and it has offered good results, also in this case [73].

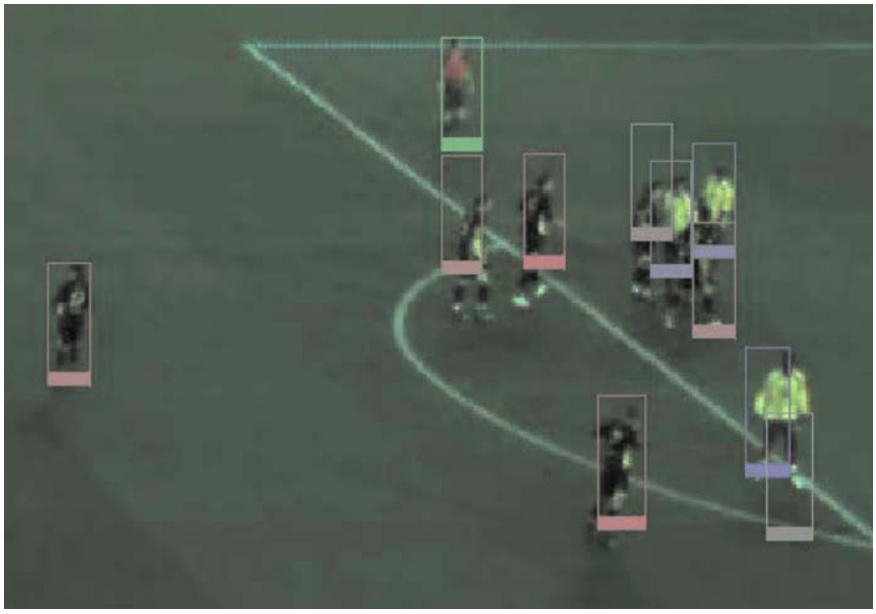

Figure 4.48 Correct Detection of football players by clustering

4.5 OPTICAL FLOW

An optical flow algorithm estimates the 2D flow field from image intensities, which is the perspective projection onto the image plane of the true 3-D velocity field of moving surfaces in space [74], arising from the relative motion of objects and the viewer. Moving objects can be separated from the background by analyzing this motion [75]. It is worth noting that the Optical flow only requires electro-optical sensors measurement to evaluate kinematical behaviour of objects, without any need of navigation system measures.

In particular, two techniques were implemented and tested in this study, which are the most used according to literature [13]: the Horn and Schunck's (HS) [77] and the Lucas and Kanade's (LK) algorithms [76]. Both of them are based on differential solving schemes. In other words, they compute image velocity from numerical evaluation of spatiotemporal derivatives of image intensities. The image domain is

consequently assumed to be differentiable in space and time. The basic assumption in measuring image motion is that the intensity structures of local time-varying image regions are approximately constant for, at least, a short time duration. This assumption brings to the following condition, known as the "Optical Flow Constraint Equation":

$$\frac{\partial I}{\partial x}u + \frac{\partial I}{\partial y}v + \frac{\partial I}{\partial t} = 0 \qquad (4.24)$$

where I represents intensity, x and y the two spatial coordinates in the image, u and v the corresponding apparent velocity components, and t is time.

This is an under-constrained equation, since only the motion component in the direction of the local gradient of the image intensity function may be estimated: this is known as "aperture problem". Therefore, one more assumption is necessary.

Horn and Schunck's method assumes that the motion field is smooth over the entire image domain. Thus, it computes an estimation of the velocity field [u, v] that minimizes both the sum of the errors for the rate of change of image brightness in eq. (4.23), and the measure of the departure from smoothness in the velocity flow [77]. Iterative equations are used to minimize equation (4.23) and thus to obtain velocity field:

$$u^{n+1} = u^n - \frac{I_x\,(I_x u^n + I_y u^n + I_t)}{\alpha^2 + I_x^2 + I_y^2} \qquad (4.25)$$

$$v^{n+1} = v^n - \frac{I_y\,(I_x v^n + I_y v^n + I_t)}{\alpha^2 + I_x^2 + I_y^2} \qquad (4.26)$$

where superscripts refer to the iteration number, subscripts refer to derivation, and α is a positive constant known as smoothness factor.

Instead, Lucas and Kanade's method divides the original image into smaller sections, Ω, assuming a constant velocity in each section. Then, it performs a weighted least-square fit of the optical flow constraint equation, to a constant model for [u, v] in each section, by minimizing the following equation:

$$\sum_{x=\omega} W^2(x)\,[I_x(x,t)u + I_y(y,t)v + I_t(x,t)]^2 \qquad (4.27)$$

where W is a weights function which basically gives more importance to the equations written near the center of the considered window ω.

The University of Naples Federico II has experimented both optical flow techniques on aerial images, acquired by visible cameras. From tests, both techniques resulted quite sensitive to background clutter, so not a reliable technique [78].

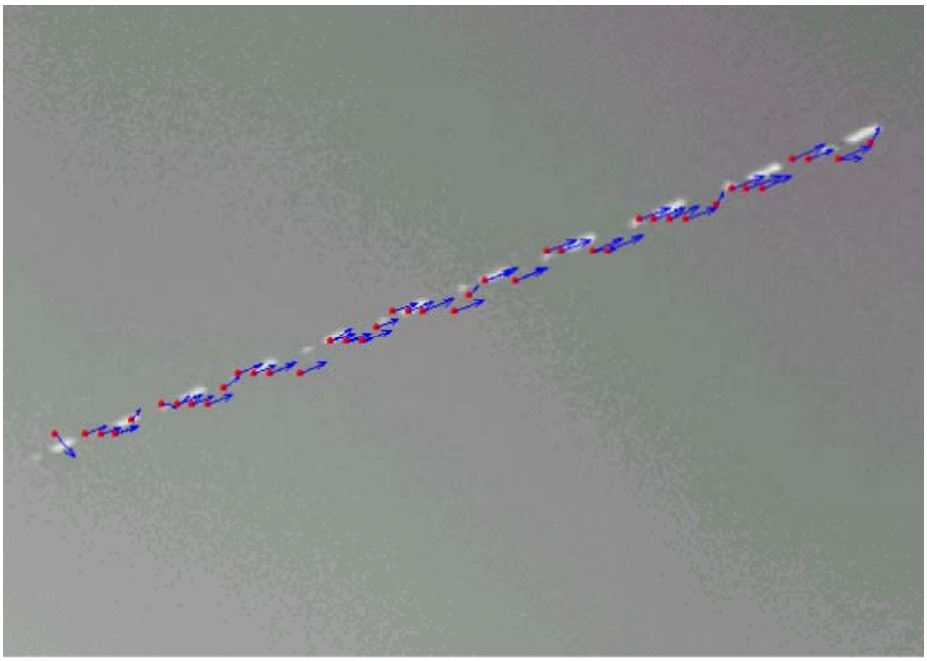

Figure 4.49 Target detected on uniform background

Thus, an alternative technique, named region-based, has been adopted by the University of Maryland and the Microsoft Research center of Washington [79]. It consists in comparing patches of the image (or filtered image) at different disparities to determine the flow. It has provided good

results in the evaluating human gesture flow, as shown in the following image.

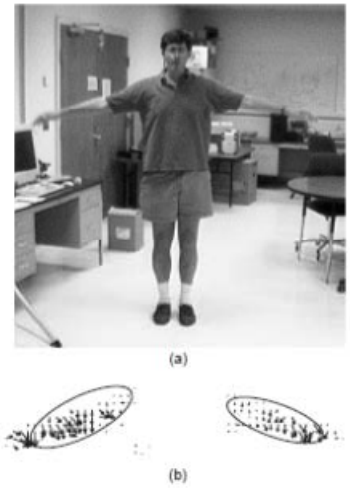

Figure 4.50 (a) Flapping action; (b) Flapping flow

4.6 MORPHOLOGICAL FILTERS

Morphology is a broad set of image processing operations that process images based on shapes. Morphological operations apply a structural element to an input image, creating an output image of the same size. However, in a morphological operation the value of each pixel in the output image is based on a comparison of the corresponding pixel in the input image with the neighbors. Thus, by choosing the size and shape of the neighborhood, you can construct a morphological operation that is sensitive to specific shapes of the input image.

Australian Aerospace research center of Queensland has been carrying out and interesting analysis of Vision-Based Detection and Tracking of Aerial Targets for UAV Collision Avoidance, based on morphological operations, which aim at highlighting potential targets [30,80].

In particular, they apply the most basic morphological operations of dilation and erosion, consecutively.

Thus, dilation adds pixels to the boundaries of objects in an image, while erosion removes pixels on objects boundaries. The number of pixels added or removed from objects in an image depends on the size of the structural element used to process the image. Combinations of simple dilation and erosion generate more complex morphological operations, named opening, an erosion followed by a dilation, and closing, the reverse.

Hereinafter we present their algebraic expressions.

Dilation:

$$I(x,y) \oplus S(x,y) = \max_{(x',y' \in S(x,y))} \{I(x-x', y-y') + S(x-x', y-y')\} \quad (4.28)$$

where I(x,y) is the processed image, S(x,y) is the structural element, while (x', y') are set by the structural element.

Erosion:

$$I(x,y) \ominus S(x,y) = \max_{(x',y' \in S(x,y))} \{I(x-x', y-y') - S(x-x', y-y')\} \quad (4.29)$$

Opening:

$$I \odot S = (I \ominus S) \oplus S \quad (4.30)$$

Closing:

$$I \circledcirc S = (I \oplus S) \ominus S \quad (4.31)$$

Indeed, Australians have experimented a Close-Minus-Open (CMO) Filter to detect aerial objects. It consists in applying subsequently the closing and the opening, such as indicated as follows:

$$CMO(I,S) = (I \odot S) - (I \circledcirc S) \quad (4.32)$$

Thus, hereinafter some results from the aerial images:

(a)

(b)

Figure 4.51 (a) original grayscale image; (b) output from CMO filtering

4.7 OBSERVATIONS AND TECHNIQUE COMPARISON

Analyzing each image processing technique, just describe in the previous sections, we can easily distinguish the most suitable methods for real-time aerial objects detection operations, which are faster than others.

However, the main requirements for vision-based aerial platforms detection are light computation load and low background sensitive. Thus, we can conclude that Sobel edge-detection, optical flow and morphological filters are the best candidates for that field of applications.

Chapter 5

TESTING STRATEGY

This chapter is mainly focused on the research experiences of the DIAS and the CIRA, concerning the SAA TECVOL project. In particular, it aims at describing the testing strategies carried out to evaluate EO obstacle detection SW performance, to tune data fusion, and to compare radar-only and multisensory intruder tracking. Indeed, two testing platforms have been used to undertake two different ways of results analysis: the hardware-in-the-loop (HWIL) facility and the FLARE platform, described in detail in chapter 2.

As regards the HWIL system, it is a laboratory test-bed, which has allowed us to work out image processing capabilities for different flight scenarios, how visible camera reacts to radar requests and its time of answer, staying in the laboratory environment, and consequently reducing exponentially the costs of experimentation.

In parallel, flight tests have been performed on the Castelvolturno (Caserta, Italy) flight field, the FLARE platform's location. During each flight a lot of data are acquired: intruder position reported by GPS and by radar; panchromatic flight images; FLARE attitude by AHRS. Those are the input data to laboratory tests, whose results anticipate

obstacle detection and intruder tracking performance of the real flying system.

5.1 HWIL LABORATORY SYSTEM

HWIL is a form of real-time simulation. HWIL differs from pure real-time simulation by the addition of a real component in the loop. One important benefit provided by HWIL platform is that testing can be done without damaging equipment or endangering lives. For instance in the automotive field, potentially damaging conditions in an engine, such as over-temperature, can be simulated to test if the Electronic Control Unit (ECU) can detect and report it. Another instance would be an anti-lock braking (ABS) simulation at performance extremes. If simulated, the performance of the ABS system can be evaluated without risk to the vehicle or operator. Moreover, in the aerospace sector laboratory test-bed are used to work out either the aerial traffic planning [81], or the UAV development life cycle [82]. However, some indoor platforms dedicated at testing UAV SAA performance have been already developed, providing many advantages in terms of costs, safety and times of experimentation [83].

5.1.1 Simulation System Setup

The detailed description of the indoor facility installed in our laboratory is provided in ref. 84 and 85. However, for the sake of clarity, we report hereinafter some structural aspects.

Thus, hardware setup is comprised of the Real World and the Simulated Hardware. The first one is represented by the visible camera, the IP-CPU, the RTT-CPU, and the hardware connections and protocols (CAN bus, Ethernet link, UDP and TCP/IP protocols). The second one is constituted by the simulators of all remaining Real World components and by the systems dedicated to the flight scenario representation: GN&C

System and Radar System Simulators, Scenario Displayer Computer, Scenario Activation Computer.

The camera is fixed to the optical bench and it processes images projected on a LCD display which is set in front of it. Both components are enclosed in a black box so that stray light effects can be neglected. In particular the monitor is connected to the Scenario Displayer Computer through a VGA connector and it shows a predefined flight scenario, activated by the Scenario Activation Computer via the Ethernet link. The Radar and the GN&C System Simulators are also activated synchronically through an Ethernet link.

Indeed, during laboratory tests data flow is the same of the real flight system: RTT-CPU receives the estimates of target position from the Radar Simulator and it transmits the relevant firm tracks estimates to the IP-CPU thus enabling the processing of the displayed images captured by the camera. If the estimated intruder position is in the camera FOV and the object detection is successfully performed, image processing will provide an improved and more accurate estimate of intruder azimuth and elevation. This estimate is then sent back to the RTT-CPU which can perform data fusion and tracking.

Figure 5.1 depicts the HWIL system architecture.

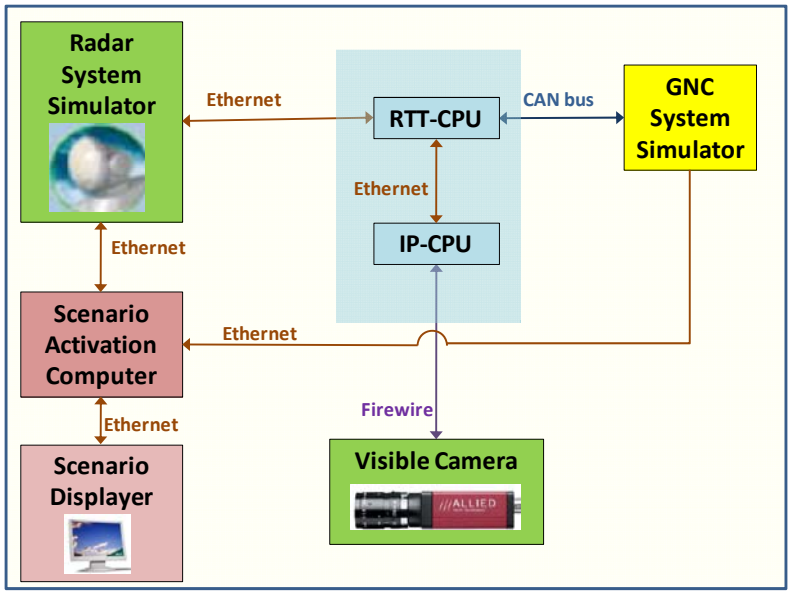

Figure 5.52 HWIL system architecture

5.1.2 Radar and Tracking

As soon as Scenario Activation Computer transmits the starting command, the Radar Simulator and the GN&C System Simulator start processing the radar measurements and own aircraft dynamics. Subsequently, in case of aerial target detection (apparent altitude higher than a given threshold), a one-plot track is initiated by the tracker that is the same used during real flights and it runs on RTT-CPU. If the track is associated with subsequent measurements, track status changes from tentative tracking and to firm tracking. The tracking algorithm makes use also of the data received by the GN&C System Simulator. In particular the latter one sends navigation data as follows: i)GPS position, ii) attitude angles and velocity components in the NED reference frame; iii) acceleration and angular velocity components in the BRF. Firm tracks data are sent to the image processing system to perform EO intruder detection.

5.1.3 EO and Image Processing

The visible camera works as auxiliary sensor to the radar system to increase the overall sensing system performance in

terms of accuracy and data rate, in fact camera resolution is 1280 x 960 pixels and it acquires 7.5 fps. These specifications allow for a system accuracy of 0.1° that is an order of magnitude less than the radar. Furthermore, EO sensors allow for a measurement update frequency of 2 Hz and more, while radar works with a data rate of less than 1 Hz.

As soon as the IP-CPU receives the estimates of the firm track from the RTT-CPU, the camera starts processing the displayed images. During HWIL tests the processing algorithm receives in input intruder range, azimuth, and elevation data in the BRF. They are converted into the CRF coordinates and compared to the camera FOV. If the estimated intruder position is enclosed in it, the image processing starts and the camera algorithm can generate an accurate intruder position reference in the CRF. In case of detection CRF estimates are converted back to the BRF and transmitted to the RTT-CPU.

The image processing algorithm has been developed on the basis of the main requirement of reduced computational load, in order to give in output a very fast answer to the RTT-CPU request. Therefore the visible camera analyzes only the image portion enclosed in the search window centered on the intruder position detected by radar, with width and height depending on intruder range. The adopted image processing technique is the coupled edge detection and labeling [52-54,89,91,92], whose choice has been already exposed in the previous chapters. Thus, it is a suitable technique for real-time applications and it is able to detect small objects such as VLAs for different illumination conditions up to about 2000 meters.

5.1.4 Display operation and scenario representation

The monitor is a 19” LCD display whose performance is described in the following table.

Table 5.8 LCD Performance

CONTRAST RATIO	500:1 (tip)
BRIGHTNESS	300 cd / m²
MAXIMUM RESOLUTION	1440 x 900 pixels

They are important for the overall system performance; in particular the monitor resolution influences the angular error of intruder representation, which considering camera-monitor distance is the order of 0.04°. This uncertainty corresponds to one pixel in the camera reference frame and as such is acceptable. Moreover monitor refresh time is significant for test execution: it exhibits good performance also at a frequency of 20 Hz, which ensures large oversampling at standard camera update rate.

Regarding the flight scenario representation, some synthetic images have been generated that replicate the real ones in terms of mean and standard deviation of the background luminance of sky and ground, with the main purpose of stimulating camera in laboratory such as during flight tests. Moreover horizon line fluctuations and intruder dynamics are simulated independently from the background, on the basis of the selected flight configuration.

Also in this case, the technique considered to realize the synthetic images from the real ones is the edge detection. In this case it has been used to detect the gaps of luminance in the entire real image, and then gaps have been replicated in a new image of LCD monitor maximum resolution dimensions (1440 x 900 pixels).

The second simulated feature is the horizon line displacement caused by FLARE attitude motion. Horizon position is calculated considering height, pitch and roll of FLARE aircraft; in particular, referring to Figure 3, the

coordinates (x_1, y_1) and (x_2, y_2) of the end points of the horizon line (whose length is 2a) in the image are given by:

$$x_1 = -a\,cos\alpha; \qquad y_1 = -(\beta_0(h) + \beta + a\,sin\alpha) \tag{5.1}$$

$$x_2 = a\,cos\alpha; \qquad y_2 = -(\beta_0(h) + \beta - a\,sin\alpha) \tag{5.2}$$

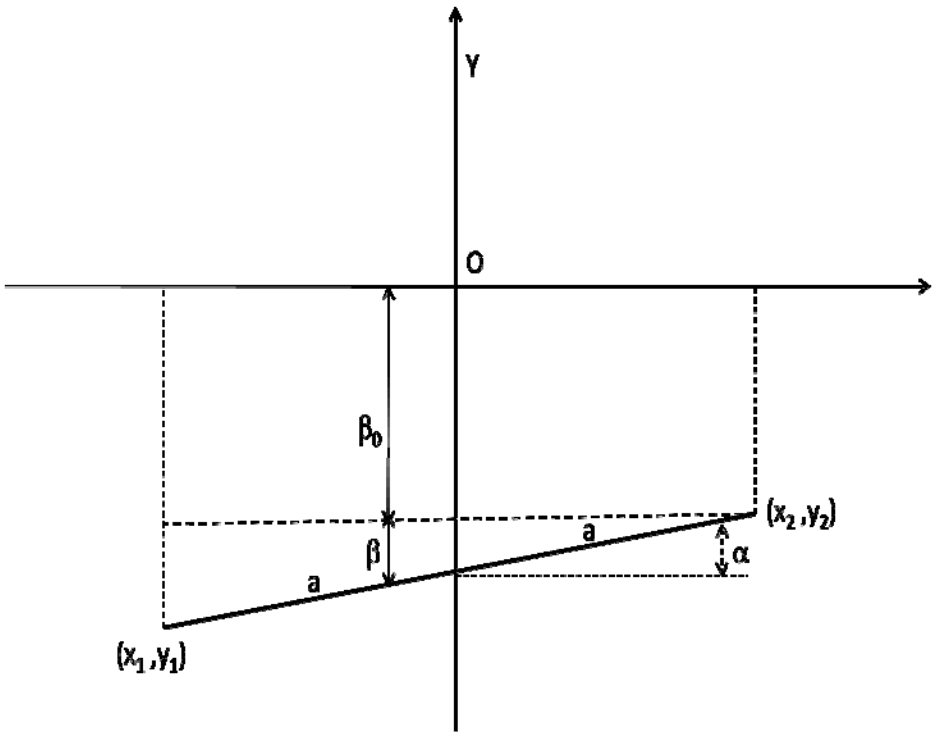

Figure 5.53 Horizon Line Representation

where h, α and β are height, roll and pitch FLARE angles respectively, while β_0 depends on the height [86]. The effective position of the horizon line on the LCD display is also based on the intrinsic camera parameters and the external calibration between camera and monitor which allows finding the connection between the CRF and the Display Reference Frame (DRF). The first ones, such as focal length, skew coefficient and distortion coefficient, have allowed for correcting all geometric optical deformations [87]; the second one have

provided the direct correlation between camera image pixel and monitor pixel, on the basis of the rigid motion equation:

$$X_c = R_c * X_d + T_c \tag{5.3}$$

in which R_c is the rotation matrix, T_c is the translation vector, X_c and X_d are the position vectors of the considered pixel in the CRF and in the DRF, respectively (see figure 5.3) [45].

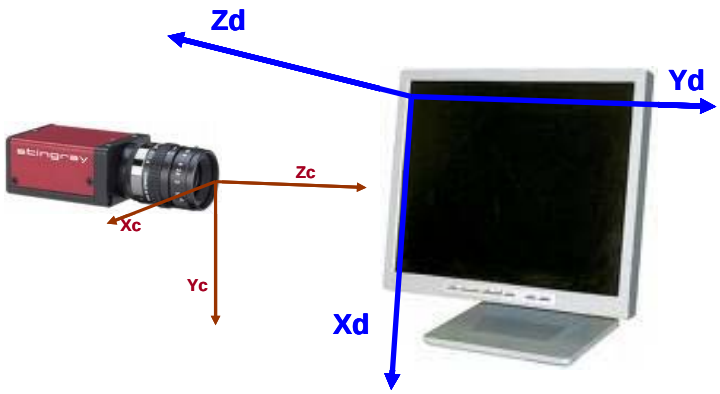

Figure 5.54 CRF with respect to DRF

An example of the synthetic background image is represented in figure 5.4.

Figure 5.55 Example of Synthetic Background Image

The last simulated real image feature is the intruder aircraft. In particular it is represented by the shape of figure 5.5, which reproduces the geometric invariants of a real intruder aircraft as estimated from flight images, up to the second order [88], with an error of 0.13%. Moreover, its

luminance coincides with the mean luminance of the real aircraft.

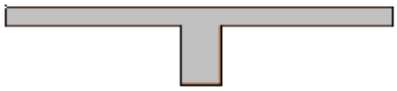

Figure 5.56 Simulated Intruder Shape

5.1.5 Optical System Setup

As already stated above, a test can be initiated as soon as the Scenario Activation Computer sends the "run test" command to the others CPU, i.e. the Radar Simulator, the GN&C System Simulator and the Scenario Displayer Computer. Subsequently, each of them starts processing the same scenario. In particular, the intruder is represented on the monitor if it is enclosed in the camera FOV.

Moreover, an appropriate collimation lens has been sized and set between camera and monitor, on the optical bench so that luminance uniformity could be guaranteed. Figure 5.6 shows the camera, the monitor and the collimator on the optical bench; then two pictures of the black box which contains all the components are reported (figures 5.7a and 5.7b).

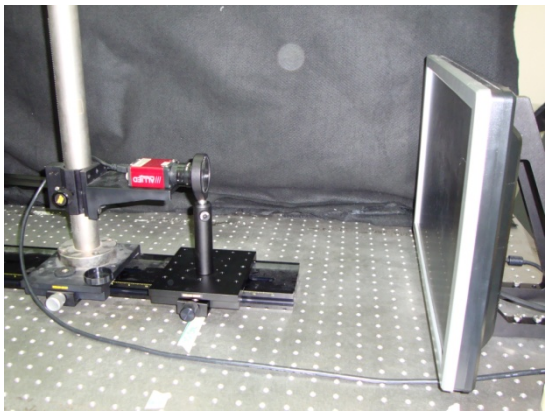

Figure 5.57 Camera-Collimator-Monitor relative disposition on Optical Bench

(a) (b)

Figure 5.58 Black Box

5.1.6 Operating Modes

The indoor facility can operate in two operating modes, such as pre-recorded and simulated flight scenario. Therefore, it allows verifying real-time performance of image processing, data fusion and tracking algorithms on the basis of acquired flight data. On the other hand, system performance can be evaluated also in different flight configurations, which are often difficult or very expensive to realize. In particular, in the case of pre-recorded flight data, intruder position is known with a frequency of 1 Hz (GPS update rate), so that the scenario displayer computer performs an interpolation of intruder range, azimuth and elevation in order to generate images at a frequency of 10 or 20 Hz.

5.2 RESULTS FROM HWIL TESTS ON THE BASIS OF FLIGHT DATA

Several HWIL experiments have been carried out in order to tune the radar-based tracking algorithm and the image processing software and to verify their reliability and real time capabilities. Results referring to tests based on flight data are reported in this section. In particular, they are related to a near collision geometry between FLARE and the intruder aircraft; therefore, the distance between the two aircrafts decreases while they fly at almost the same altitude. In this flight phase the tracker operates in firm

tracking mode due to the quite large number of intruder echoes detected by the radar. Tracker output constitutes the input data for the image processing algorithm, which outcomes a more accurate intruder position.

Figures 5.8a-d show the image processing algorithm applied to an image acquired by the camera during the HWIL test, and figures 5.9a-c report the radar-only and EO detection results in range, azimuth, and elevation in the BRF, compared to relative geometry computed in post-processing from GPS/AHRS data.

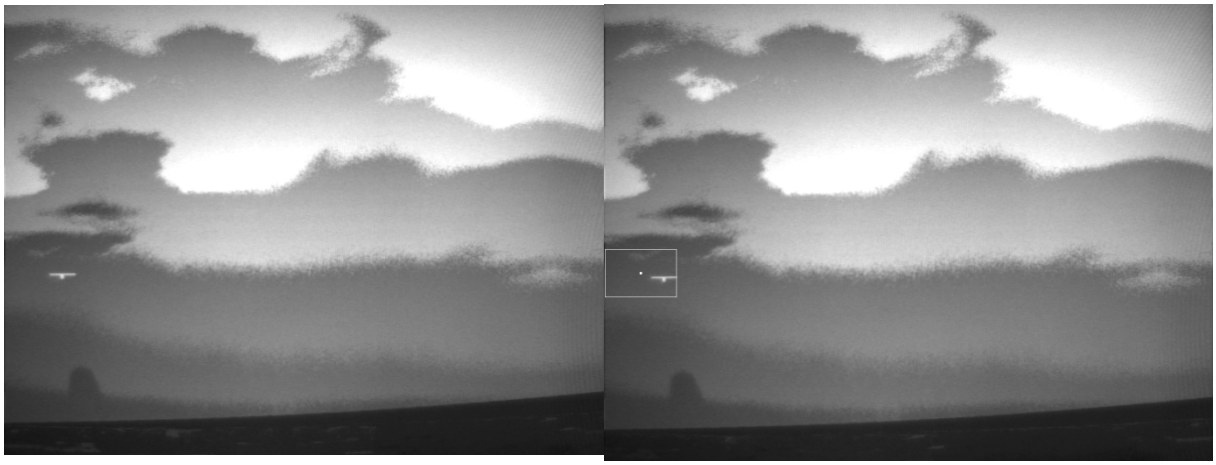

(a)

(b)

(c)

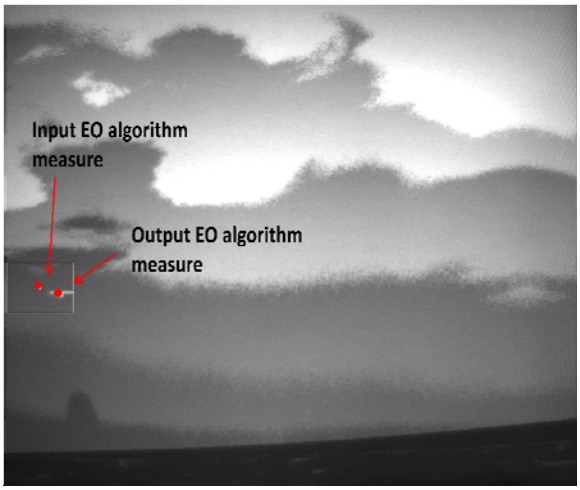

(d)

Figure 5.59 (a) Instantaneous Acquired Image; (b) Search Window built on the basis of Radar-Only Tracking Measurements; (c) Image Processing Algorithm applied to the search window; (d) Comparison between tracker EO input and EO output

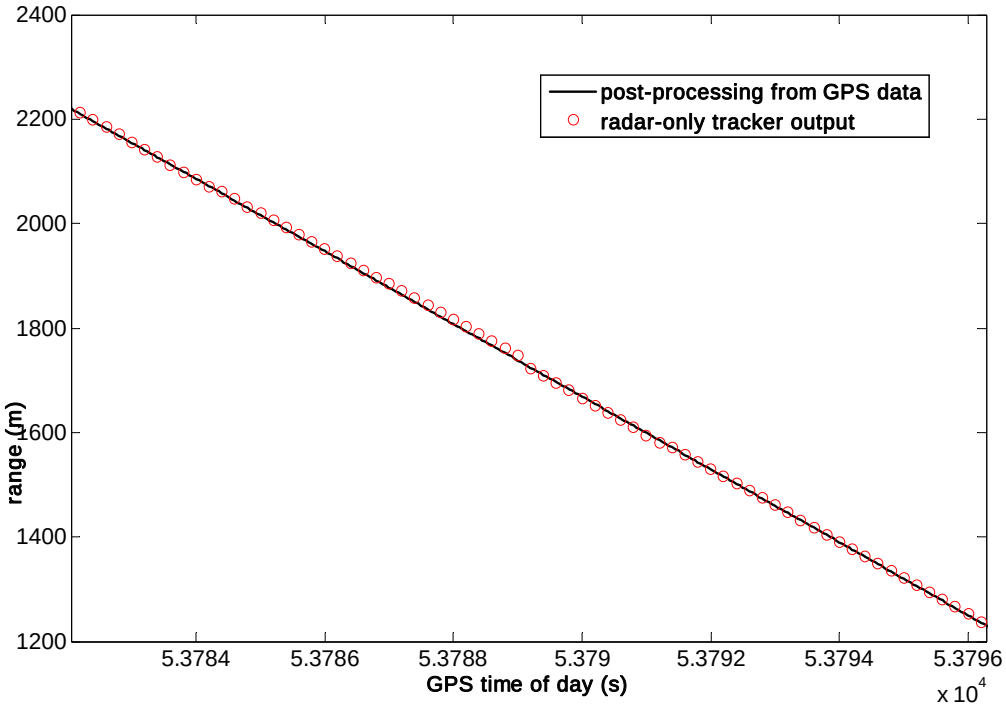
post-processing from GPS data
radar-only tracker output
range (m)
GPS time of day (s)
x 10^4
2400
2200
2000
1800
1600
1400
1200
5.3784
5.3786
5.3788
5.379
5.3792
5.3794
5.3796

(a)

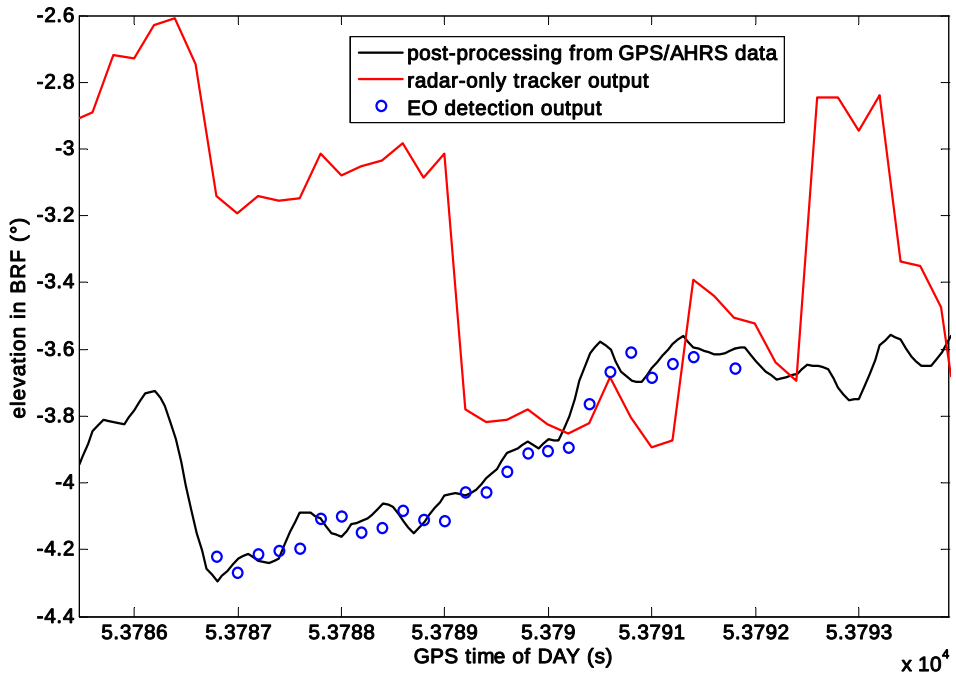
post-processing from GPS/AHRS data
radar-only tracker output
EO detection output
elevation in BRF (°)
GPS time of DAY (s)
x 10^4
-2.6
-2.8
-3
-3.2
-3.4
-3.6
-3.8
-4
-4.2
-4.4
5.3786
5.3787
5.3788
5.3789
5.379
5.3791
5.3792
5.3793

(b)

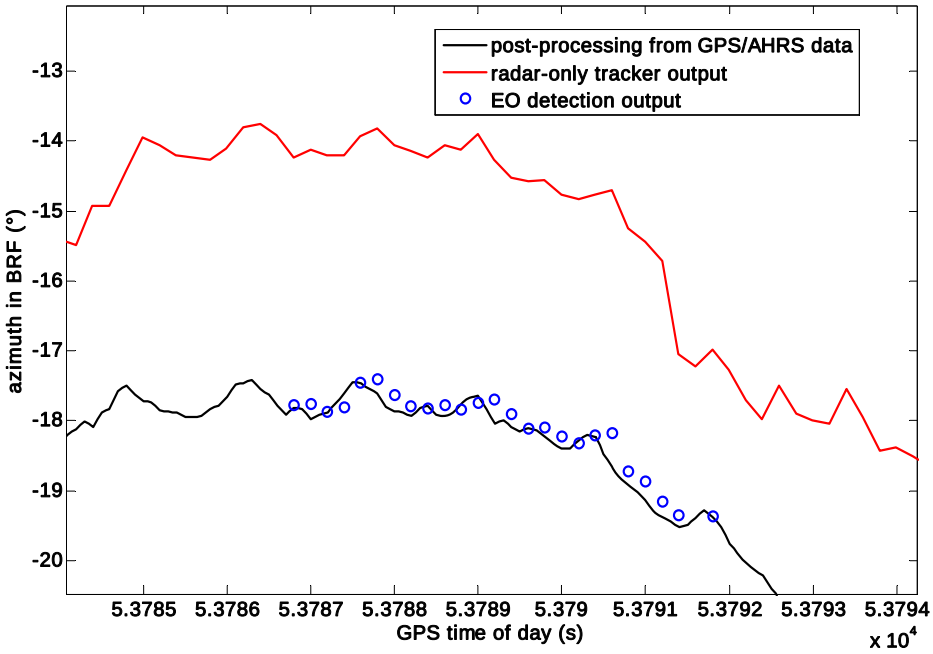

(c)

Figure 5.60 (a) Comparison of intruder range as estimated by GPS and by Radar-only Tracking; (b) Comparison of intruder elevation as estimated by GPS/AHRS, by Radar-only Tracking and by the EO System; (c) Comparison of intruder azimuth as estimated by GPS/AHRS, by Radar-only Tracking and by the EO System.

The quality of the obtained results confirms the good synchronization obtained in the laboratory tests. The range diagram (figure 5.9a) shows that the tracker has attained a very high accuracy level which directly derives from the radar sensor. The elevation diagram (figure 5.9b) illustrates that the EO detection output is more accurate than the radar-only tracking one and it corrects the radar error bias which is due to residual misalignment between radar and AHRS. Of course, the capability to remove this bias in flight experiments depends on the accuracy of cameras-AHRS alignment onboard the aircraft, which indeed has been demonstrated to be of the order of 0.1° in reference no. 40. In particular, the error standard deviation in EO estimates is one order of magnitude smaller than radar one, as it was expected from the off-line analysis of flight images. A similar result can be observed in figure 5.9c which represents azimuth plot. It is worth noting that the radar outputs useful measurements, i.e. measurements

that can be associated with the intruder, at a frequency in the order of 1 Hz or less, whereas the EO detection estimates are at a frequency of 5 Hz.

Finally, table 5.2 synthesizes EO detection performance evaluated in the real-time tests by reporting error mean and standard deviation. It demonstrates that this performance is fully compliant with the requirements.

Table 5.9 EO Real-Time Detection Performance in terms of error mean and standard deviation

	μ_ε (°)	σ_ε (°)
Azimuth	$3.0\ 10^{-3}$	$1.2\ 10^{-1}$
Elevation	$2.2\ 10^{-3}$	$7.0\ 10^{-2}$

An important point is related to latency in image processing for obstacle detection. From this point of view, performed tests revealed a latency of less than 0.1 s (mean value 85 ms). This result is shown in figure 5.10 which reports the epochs of tracker requests and related image processing estimates.

The main limit of HWIL analysis regards the difficulty to evaluate the false alarm and miss detection rate of the image processing algorithm. In fact, these ones mainly depend on the illumination distribution in the flight scenario. From this point of view, the simulation still needs to be improved to reproduce the one acquired in real conditions. As a consequence, it is not possible to study the trend of EO detection range for the different conditions. At the moment, all these analyses have been carried out off-line, and will be explained in the following chapter.

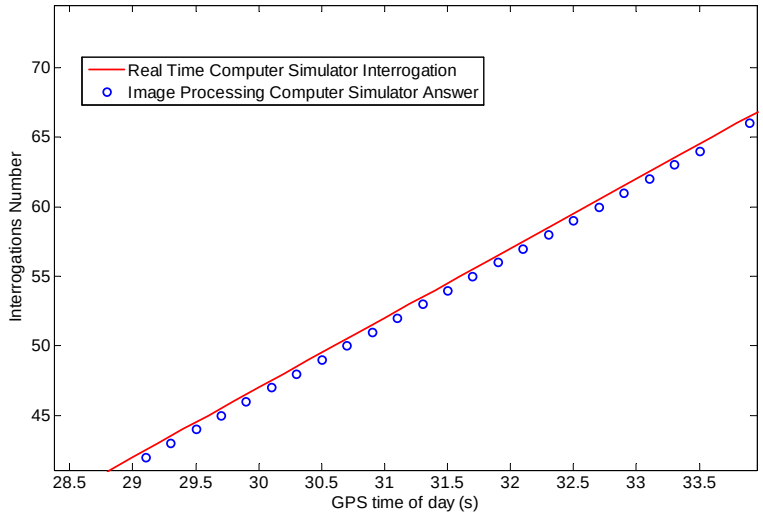

Figure 5.61 Times of tracker requests and image processing answers.

Thus, the main advantage provided by HWIL facility is to have allowed us to test the camera capability of performing obstacle detection in the required by radar time and to evaluate image processing algorithm reliability in good luminosity background conditions. Indeed, HWIL results have demonstrated that EO system is able to work out the intruder position very accurately, and its frequency of measurements can increase the overall DS&A system data rate from three to five times with respect to the radar-only system configuration. So, results prove that main EO cameras requirements, expressed in chapter 3, are fulfilled.

5.3 FLIGHT TESTING STRATEGY

Several flight tests were carried out to gather radar and electro-optical data and to estimate system performance. In particular, they permitted to asses several features of the system that cannot be properly modeled by numerical or laboratory tests, such as the effect of ground clutter and background on both radar and EO sensors, the effects of sun

illumination changes, and all secondary sources of error that are present in real platforms and that are not easily accounted for in standard level simulations, such as vibrations and electromagnetic interferences.

Flight tests were performed by exploiting the following configuration of test facilities:

- FLARE aircraft piloted by human pilot or by the autonomous flight control system with the fully installed and functional setup described in the previous sections;
- A piloted VLA aircraft in the same class of FLARE equipped with GPS;
- A Ground Control Station (GCS) for real-time flight coordination and test monitoring [90];
- A full-duplex data-link between FLARE and GCS. This data-link allowed GCS operators to send commands to initiate or terminate tests and to receive synthetic filter output and navigation measurements. Indeed, no workload was assigned to human pilot in terms of sensor unit management in flight;
- A downlink between intruder and GCS. This data-link was used for flight monitoring.

During the tests autonomous anti-collision logic was not engaged, since the focus was set on sensor system development and performance estimation. Two types of maneuvers were basically executed during flight experiments:

1. Chasing tests with FLARE pursuing the intruder. These tests were performed in order to estimate tracking performance for long time duration with negligible miss detection rate. Moreover, chasing phases can be effectively used to estimate residual radar misalignment with respect to AHRS thanks to the large number of intruder detections, smooth relative dynamics, and consequent small impact of latencies. For this reason, the

two aircraft started their routes from the closest point that is compatible with safe flight and they continued their straight flight increasing the relative distance. This condition was achieved by assigning a small speed excess to intruder aircraft;

2. Quasi-frontal encounters. These tests were performed to estimate detection and tracking performance in real scenarios. The two aircraft started the test from furthest points within the data-link coverage area. They followed quasi-collision trajectories on parallel routes or on routes that formed a small angle. Different relative flight level configurations were assigned to the aircraft depending on the expected ground clutter level.

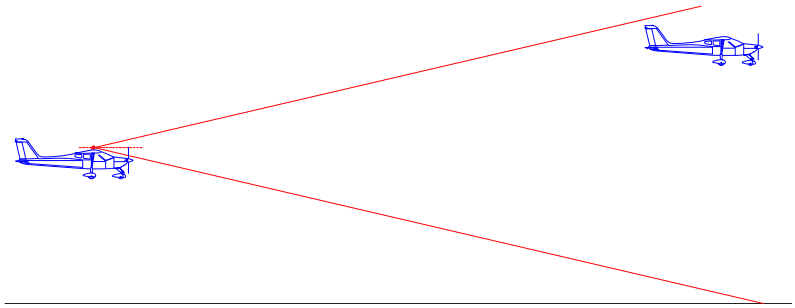

(a)

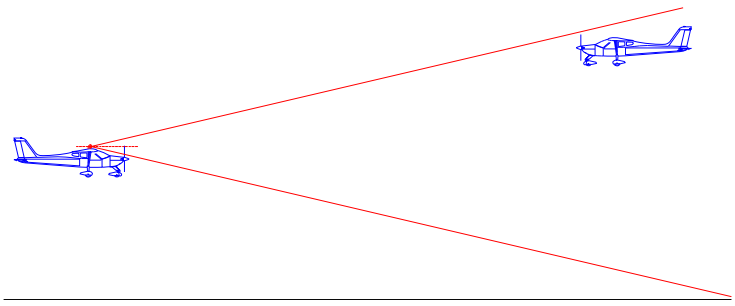

(b)

Figure 5.62 (a) Chasing Configuration; (b) Quasi-frontal encounter.

Chapter 6

IMAGE PROCESSING ALGORITHM RESULTS

HWIL analysis has allowed us to test real-time performance of the edge detection-labeling algorithm, realized for the panchromatic camera in the framework of the TECVOL DS&A project. Thus, good results have been obtained, in terms of times of answer to radar's requests, data rate measurements, accuracy of intruder position estimates. Indeed, an off-line analysis, conducted on the real images acquired during flight tests, is needed in order to evaluate image processing algorithm performance in more different luminosity and background conditions and to study its reliability in a realer context.

However, this chapter is dedicated to the description of that off-line analysis, and the customization of the image processing technique, worked out to guarantee the best results in terms of detection range, missed detection rate, and false alarm rate. Lastly algorithm performance is evaluated, confirming again the importance of the EO sensors in the overall DS&A system: the improvement in terms of accuracy and data rate, compared with radar-only tracking, is quantitatively demonstrated.

For more clarity, the reader can refer to paper number 93 of References.

6.1 SELECTION OF THE BEST IMAGE PROCESSING TECHNIQUE

The image processing algorithm selection for the panchromatic camera has followed a detailed comparison of the main techniques listed in literature, whose description has been already reported in detail in chapter 4. It has aimed at evaluating the best algorithm in terms of computational load, detection range, false alarm and missed detection rates, and adaptability to various background brightness and illumination conditions.

From all techniques, the best candidates for real-time object detection have resulted optical flow, binarization, coupled edge detection and labeling, and morphological filters. Thus, clustering is too slow and corner detection is not suitable for our research application.

Indeed, also optical flow and morphological filters have been discarded: the first is not ideal for our system, because it characterized by a maximum acquisition data rate of 7.5 fps. In fact this low date rate provides the pixel displacement speed major than 1 pixel per frame, which is an optical flow technique requirement [79]. Moreover, the morphological filters operators are very effective for standalone EO sensors, which is a DS&A system configuration different from ours, where they are auxiliary to radar.

Thus, the comparison has been conducted between binarization and edge detection.

The binarization technique has been applied to several image sequences taken during flight tests, in order to evaluate the best threshold for isolating the intruder aircraft from the background noise. $\mu \pm 3\sigma$ resulted as the best choice for our application on the basis of statistics on images acquired

during flights. In the above reported criterion, μ is the mean intensity of the considered search window, while σ is its standard deviation. Assuming a Gaussian distribution of pixel intensity in the search window, this threshold corresponds to an estimated probability of 99,7%. As it will be better clarified in the following, the main drawback of the binarization technique has been demonstrated to lie in its unsatisfying performance for non-homogeneous background.

Finally, the implementation of the edge detection-labeling technique is carried out following a stepwise procedure, such as:

- Building of the search window on the basis of the radar estimates, as already explained in the previous section;

- Search window binarization by means of the Sobel edge detection technique [53,54,89]. In order to limit the impact of background noise, a relatively high threshold has been considered in Sobel method, on the basis of the assumption that the intensity gradient generated by the intruder is larger than the other background objects. More details about threshold selection are discussed in the following;

- Implementation of the labeling technique which connects all detected pixels in the binarized search window (if any) and outputs a limited number of edges;

- Detection of the intruder aircraft as the largest edge, i.e., the edge that is comprised of the greatest number of pixels.

For the sake of concreteness, figures 6.1 and 6.2 illustrate the implementation of the adopted method and its output on a flight image taken during a frontal encounter phase.

(a)

(b) (c)

Figure 6.63 (a) Flight image with the search window centered on input radar-based tracking estimates; (b) processed image; (c) edge detection–labeling algorithm output.

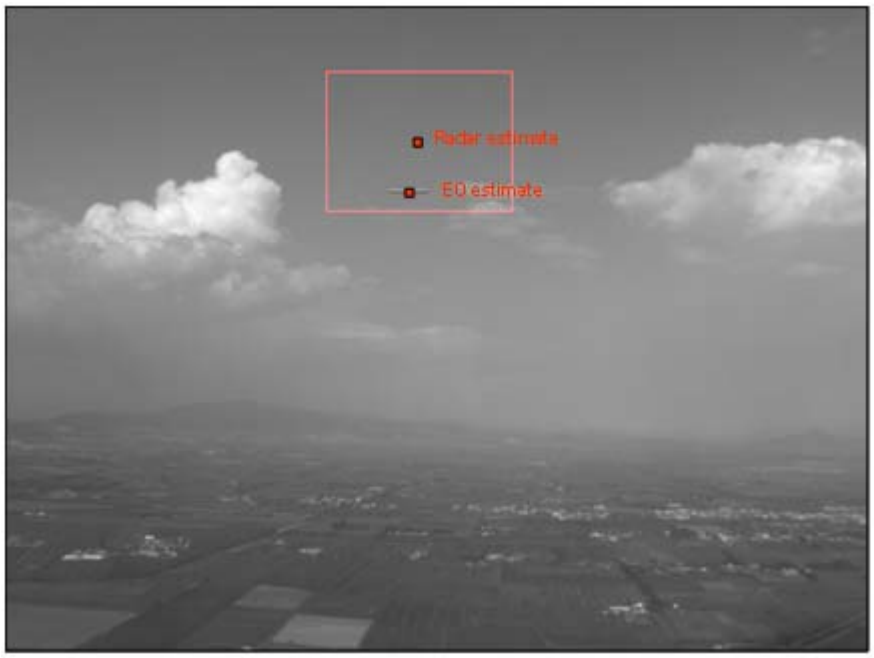

Figure 6.64 EO intruder position detection compared with radar-based tracker estimation.

Finally figure 6.3 shows the edge detection-labeling technique applied on a search window which encloses the intruder aircraft at a range of 2400 meters.

(a) (b)

Figure 6.65 (a) Output of the image processing technique applied on the search window; (b) Intruder aircraft detected at 2400 m.

Two important points for algorithm implementation are relevant to the dimensions of the search window and the choice of Sobel threshold. They are focused in what follows.

6.1.1 Search window dimensions

Search window definition has to take into account several aspects. First of all, window dimensions have to be set considering uncertainty sources such as radar error in NED and residual time/space registration errors. On the other hand, at relatively small range the search window has to be large enough to enclose the largest possible obstacles. Finally, window dimensions cannot increase too much because of the consequent computational weight of obstacle detection techniques.

Thus, search window dimensions are defined as follows. When the estimated intruder range is larger than 350 m, the window has constant dimensions in pixels, i.e. 150 (width) X 100 (height) pixels, corresponding to an angular FOV of about 6° X 4°. Of course, linear dimensions of the search window increase for increasing range and are always large enough to enclose a typical civil aviation aircraft, such as a Boeing 737 or an Airbus A320. In order to set a lower bound for search window dimensions, when the range is smaller than 350 m the window dimensions in pixels are inversely proportional to range thus achieving constant linear dimensions. Indeed, these cases are of little interest for sense and avoid applications.

Figure 6.4 depicts linear dimensions (in m) of the search window as a function of the estimated intruder range.

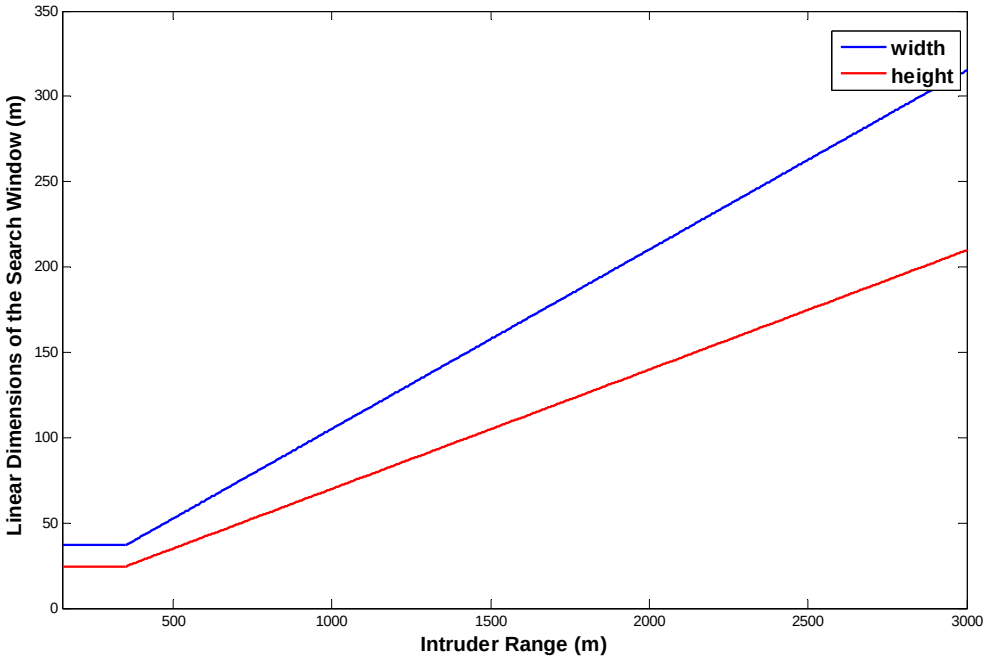

Figure 6.66 Search Window: law of variation

6.1.2 Sobel threshold

As regards the choice of the Sobel threshold, it is not fixed, but it changes as a function of the estimated intruder range. The most effective thresholds able to distinguish the intruder from the background have been calculated by an empirical analysis based on the large amount of images taken during flight tests [94]. It has resulted that the most suitable threshold applicable at the intensity gradient magnitude increases when intruder range reduces and it changes from about 39 to a maximum value of 42. These results are explained in the following figure which reports an example of histogram of gradient magnitude in the search window and depicts the thresholds applied on three different intruder range cases (low, medium and long range). Indeed, the reader can observe that the histogram has a Rayleigh distribution, being in accordance with Voorhees and Poggio theory [95].

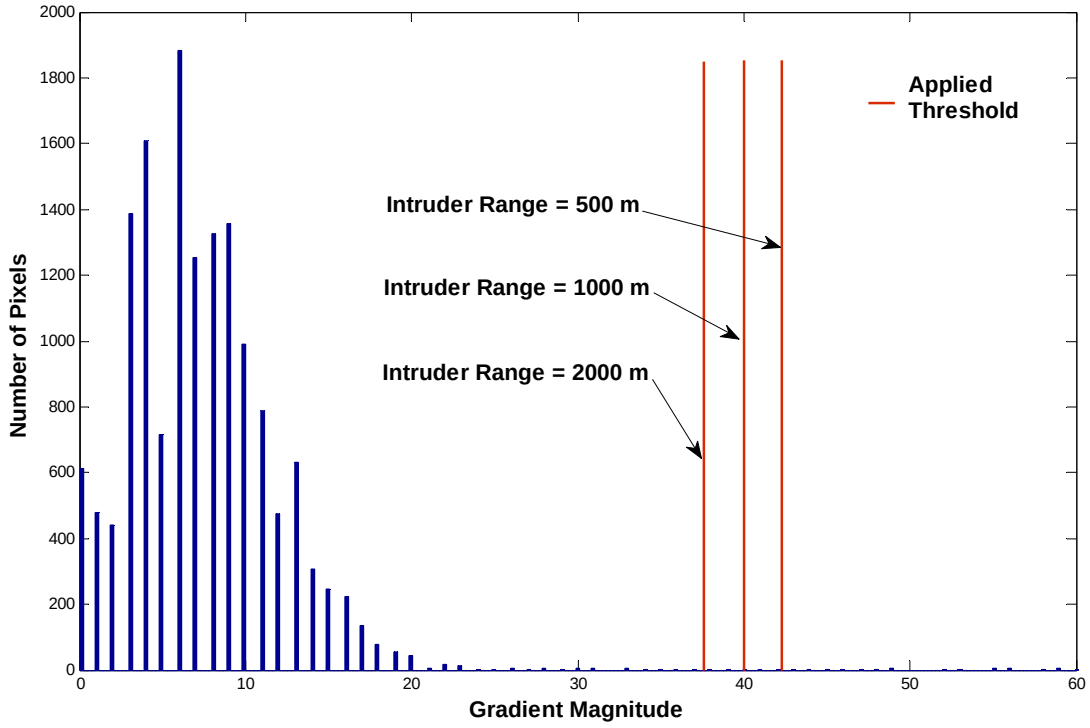

Figure 6.67 Threshold versus Intruder Range

Moreover, evaluating the probability density function (pdf) of our Rayleigh curve, we obtain it is directly proportional to intruder range, standing for the increasing of false alarm probability parallel to the range. However, figure 6.6 illustrates the pdf variation in function of the intruder range and it demonstrates that the probability of false alarms is very low, less than 10^{-8}, for the entire threshold slot.

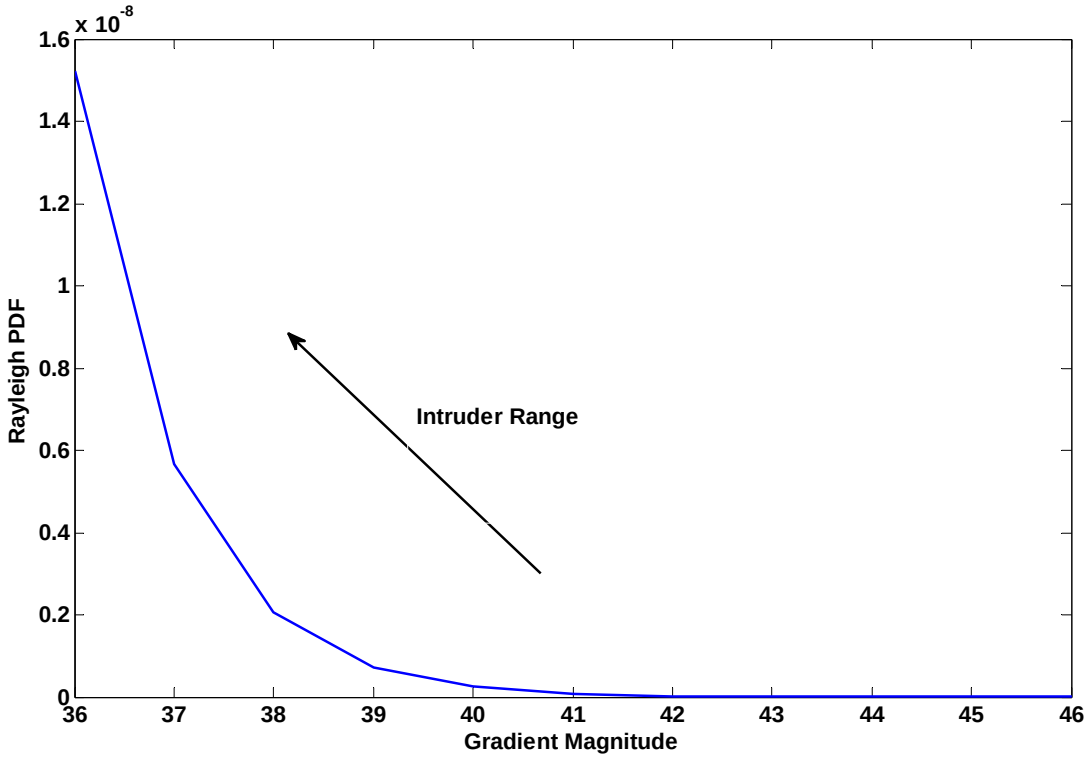

Figure 6.68 Rayleigh pdf distribution of Search Window Background

6.2 PERFORMANCE ASSESSMENT AND FLIGHT RESULTS

In order to compare the two candidate image processing techniques, they have been applied to the same sequence of images taken during near collision encounters in the performed flight tests. Indeed, we have obtained the results reported in table 6.1.

They can be summarized as follows:

the binarization technique has good performance in terms of computational load, false alarm rate, and missed detection rate for brightness conditions of homogeneous backgrounds. Indeed, its performance is degraded for inhomogeneous backgrounds and the relevant detection range of VLA doesn't overcome 1 km;

on the other hand, the edge detection-labeling technique reveals good performance for all requirements, both in terms of detection range and reliability, in fact it is able to detect VLA as far as 2400 m.

Therefore, the edge detection-labeling overcomes the binarization in all considered aspects, except for the computational load which is almost equal for both. The computational load and real time performance was evaluated by means of the laboratory system facility described in the previous chapter [84,85].

Table 6.10 Performance Comparison of image processing techniques relevant to frontal encounters carried out during flight tests

Technique	False Alarms (%)	Missed detections (%)	Correct Detections (%)	Initial detection range (m)	Computation Time on the IP-CPU(ms)
Binarization	32	54	13	930	< 100
Edge Detection - Labeling	9	12	80	2400	< 100

After this first performance estimate, the edge detection-labeling algorithm has been refined with the aim of drastically reducing false alarm rate in spite of increasing missed detections [96]. Since the camera output is used to improve the accuracy of the tracker that is based on the radar as primary sensor, it is preferable that the IP-CPU outputs to RTT-CPU fewer, but more reliable EO measurements in order to enhance the overall system tracker performance. In fact, the main effect of a missed detection is to reduce EO measurement rate and thus the algorithm capability to filter sensors noise and improve estimation accuracy, especially on angular derivatives. Instead, if a false alarm falls inside the track gate, disassociation occurs and, due to the small EO

measurement covariance, it can have dramatic consequences for tracking reliability such as biases generation and then track loss.

In particular the critical situations for false alarms risks can be classified in two main categories: presence of sun glares in the captured image, and horizon presence in the search window.

For the first case a "Sun Presence Detector" has been implemented. It evaluates the percentage of saturated pixels of the whole image and it is based on a statistical study applied on real images. From results it has been always verified that when sun is in front of the camera, more than 15% of the pixels are saturated. This percentage is the reference threshold considered by the detector; if the sun is detected, the edge detection algorithm is not run and the IP-CPU doesn't send any EO measurements to tracker.

An example of sun detector implementation is shown in figure 6.7.

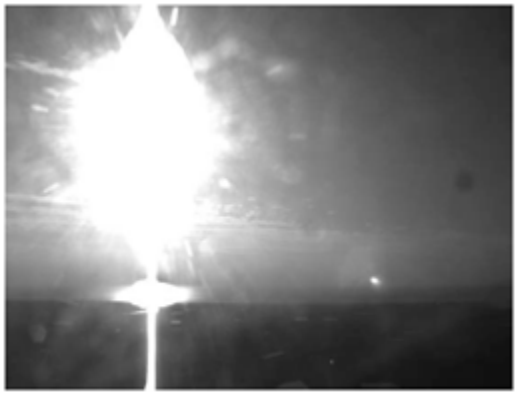

Figure 6.69 Sun presence detected by "Sun Detector"

Horizon presence in the search window is handled in different ways depending on intruder range. In particular, after edge detection-labeling, a further filter is implemented in order

to compare the largest edge length to the instantaneous intruder range and to evaluate the probability that it is an intruder or background noise. The reference lengths are the wing span of a civil aviation aircraft (B737) as well as the wing span of smaller vehicles such as the TECNAM P92. They are calculated at different ranges, taking into account also the extension atmosphere and height effects [55], and explained by the following equation:

$$C_R = e^{-\sigma_v(h) * R} \tag{6.1}$$

Where C_R is the attenuated length in percentage, R is the object range from the point of observation, and σ_v is the attenuation factor, depending on the object altitude h. Our flight tests happen usually in "haze" atmosphere [55]. Therefore, the value of σ_v is attenuated when altitude increases from sea-level on the basis of the following curve, replicated from ref. 55:

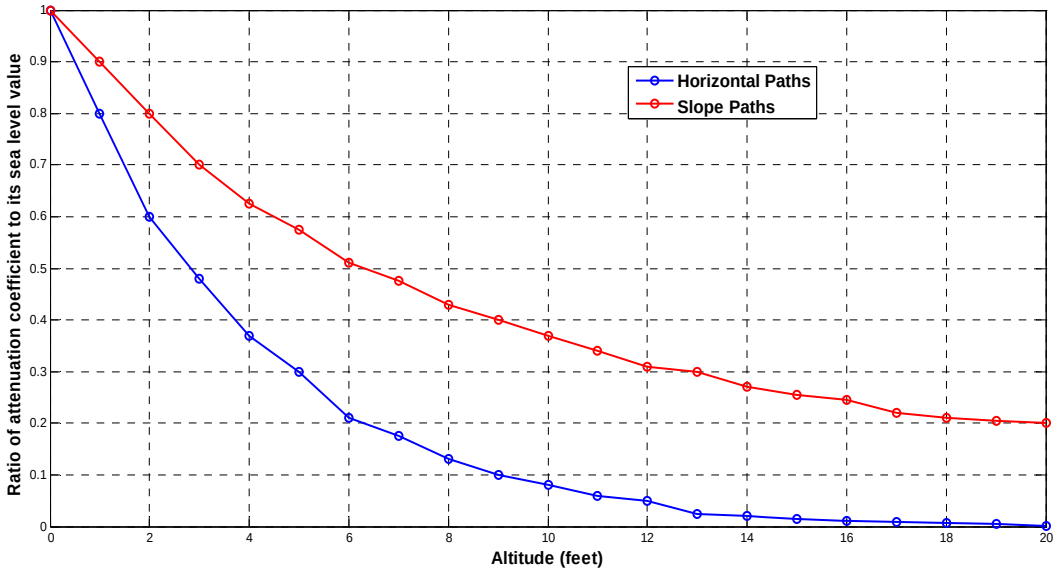

Figure 6.70 Altitude Effects on Atmospheric Attenuation Coefficient

Therefore the edge detection output is declared as intruder if it is enclosed in the range of reference wing spans. Secondly, the algorithm provides a higher-level control during which

assures that the detected edge has no comparable segments, otherwise it doesn't output any intruder position measurements

An example of horizon presence in the search window and of the resulting edge detection output is reported in figures 6.9.

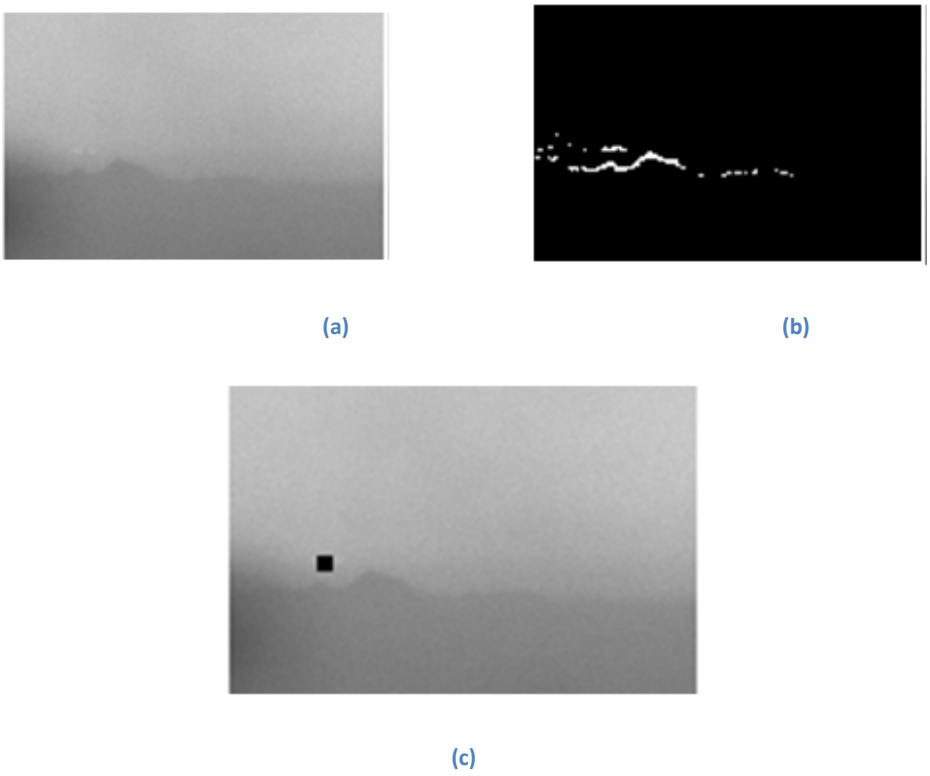

(a) (b)

(c)

Figure 6.71 (a) Search window enclosing horizon; (b) Edge detection-labeling implementation; (c) Image processing algorithm output.

Applying these controls of false alarm risks, the edge detection-labeling method provides new performance synthesized in Table 6.2.

Table 6.11 Edge detection–labeling performance optimized in the considered frontal encounters

Technique	False Alarms (%)	Missed Detections (%)	Correct Detections (%)	Initial Detection Range (m)	Computation Time of IP-CPU(ms)
Edge Detection – Labeling	1.6	37.6	60.8	2400	< 100

It is important to point out that these results are compliant with tracking requirements expressed in terms of false alarms rate, computational time, and detection range.

Moreover, figures 6.10 and 6.11 show that panchromatic camera measurements allow a great improvement in both accuracy and data rate with respect to radar-only tracking, either for azimuth or for elevation angle estimates. In these cases there are no EO false alarms and every measurement from panchromatic camera falls properly into the track gate and can be fused with radar estimates by RTT-CPU.

As regards the achievable accuracy and measurement rate, because of the residual uncertainties on data synchronization and sensor alignment, average EO detection accuracy in the North-East-Down (NED) reference frame was found to be of the order of 0.5°, with a measurement rate of 5 Hz (limited by the maximum achievable frame rate at full resolution). Though these values do not represent the performance limit of the EO system, they already constitute a significant improvement compared with radar performance (1.7° angular accuracy and measurement rate smaller than 1 Hz on average). It is worth noting that real time hardware-in-the-loop tests demonstrated an accuracy of about 0.1°, as reported in chapter 5.

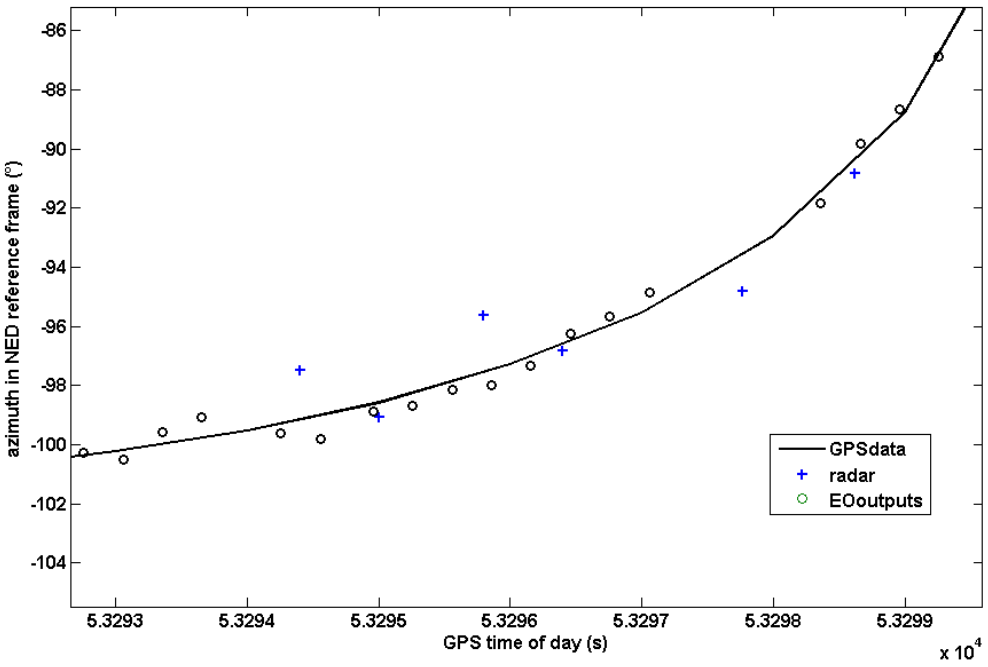

Figure 6.72 Comparison of intruder azimuth in NED reference frame among radar, EO, and the post processing of GPS data output that is used as reference.

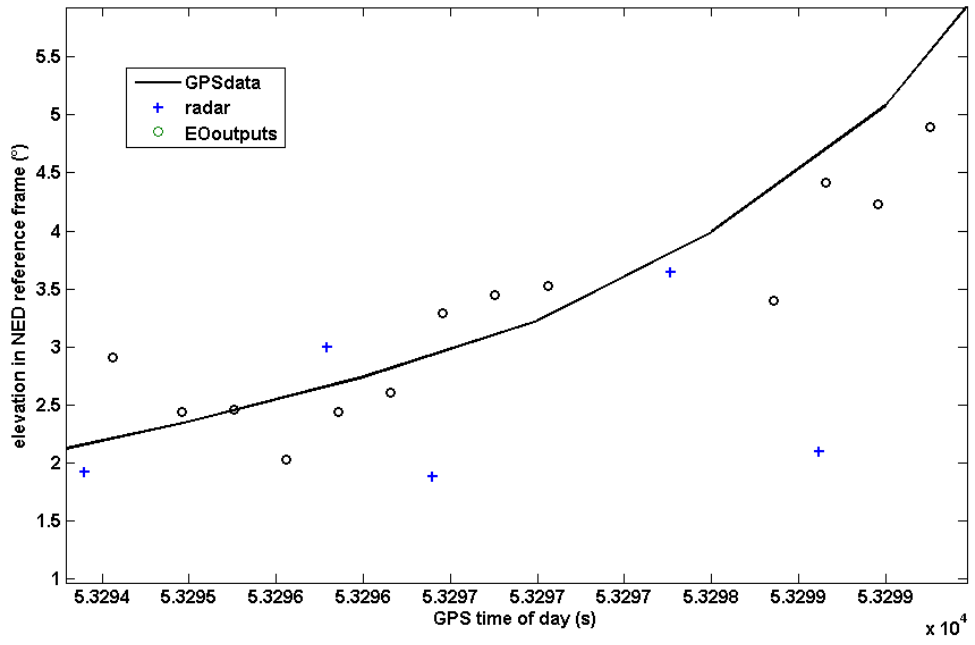

Figure 6.73 Comparison of intruder elevation in NED reference frame among radar, EO, and the post processing of GPS data output that is used as reference.

As a result of these performance levels, accuracy and reliability of the developed multi-sensor tracker can be greatly improved [91,92,97,98].

6.3 EO OBSTACLE DETECTION IMPLEMENTION: EXAMPLES

Hereinafter some examples of EO obstacle detection implementation are proposed. In particular, each of them presents the intruder aircraft at about 1500 m from FLARE platform, in three different background and illumination conditions, respectively. Thus, the purpose is to demonstrate how the algorithm is able to provide the correct estimate of intruder position for each of the considered case.

In each figure the whole image acquired by the camera, the processed search window, the result of binarization based on edge detection-labeling, and the algorithm output indicated with a blue arrow, are shown. In all three cases the arrow coincides with the actual intruder aircraft position. In detail, figure 6.12 is a flight image acquired in sunny conditions, figure 6.13 shows the algorithm implementation on a cloudy background image and figure 6.14 shows another case in which the horizon line lies in the search window, but the algorithm is able to discard it thanks to the high threshold, and to successfully detect the intruder.

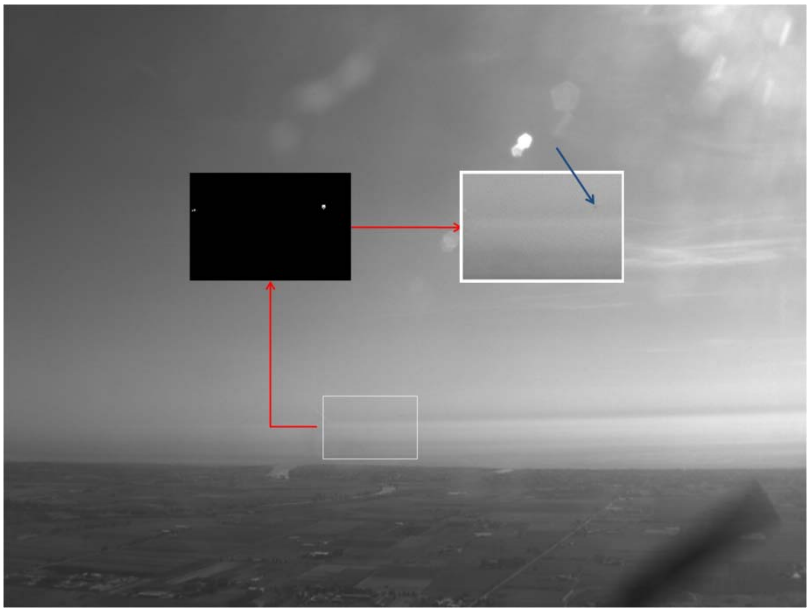

Figure 6.74 Intruder detection in a sunny image

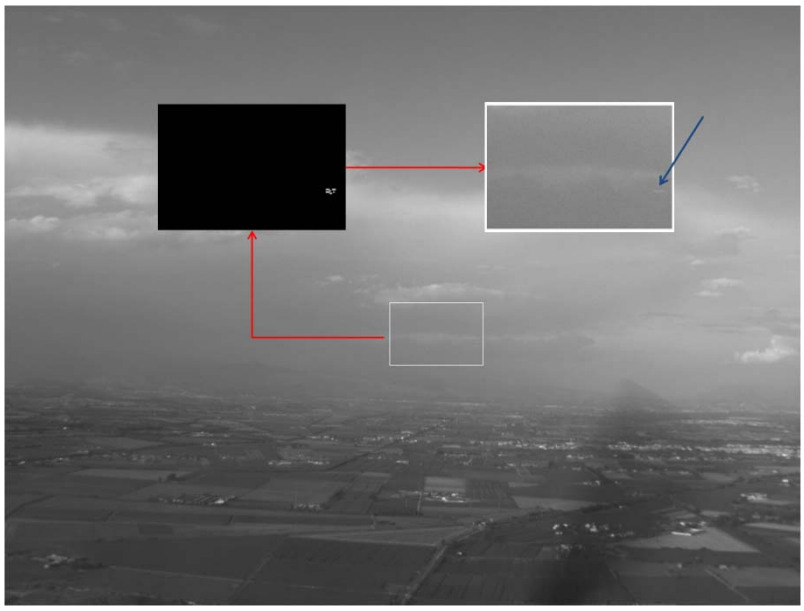

Figure 6.75 Intruder detection in a cloudy image

Figure 6.76 Intruder detection with horizon line

CONCLUSIONS AND FURTHER DEVELOPMENTS

This thesis is focused on the EO sensors of an integrated multi-sensor based non cooperative anti-collision system for UAVs. In particular, it aims at demonstrating the benefits provided by cameras to the overall DS&A system.

Thus, the sensing system is installed onboard a VLA, which is the experimental platform, and it is constituted by radar, principle sensor, and four EO cameras, two visible and two IR, that operate as secondary sensors, performing auxiliary functions to radar. That hierarchical sensor architecture comes out very strategic, in fact it takes advantage of all good EO performance, in terms of accuracy and data rate, discarding the negative aspects, such as the sensitiveness to background luminosity and clutter.

The DS&A hardware architecture is described in detail and it is worth noticing that sensing processing unit is divided into two parts: one dedicated to elaborate radar measurements and intruder tracking; another one dedicated only to image processing and connected to the other processing unit by Ethernet link. That CPU's structure is very advantageous in terms of computational load, which turns out light and quick, main requirements for real-time systems.

The main part of the thesis is dedicated to the analysis of the most common image processing techniques listed in literature and used for object detection operations. This study has been carried out in order to find out the most suitable method to our application. Indeed, the coupled edge-detection labeling technique has been chosen because it has come out very fast, accurate, with low sensitiveness to background clutter. However, two parallel ways of testing have been undertaken, with two different testing platforms, respectively: laboratory tests have been performed by means of a HWIL system, in order to verify real-time image processing performance; an off-line analysis has been pointed out on real images, acquired during flight tests, in order to evaluate object detection performance in real background clutter.

Satisfying results have been obtained from both sides: HWIL tests have demonstrated that cameras are able to elaborate images in restricted times; in fact they answer to radar's request almost immediately, so that data fusion and intruder tracking can be worked out. The off-line analysis has been advantageous to evaluate the behavior of the algorithm in different background and luminosity conditions, such as sun presence in front of cameras, horizon line, or, more in general, clutter generated by clouds in proximity of the intruder aircraft. That study has allowed us to customize the algorithm, in order to manage also these features, which can be cause of false alarms.

The study explicated in this thesis concludes with the resume of the image processing algorithm performance, evaluated from real-time and off-line tests, and based on the customized algorithm.

Thus, results demonstrate that EO system fulfills the expected object detection performance; indeed, it allows the overall DS&A system to increase intruder position accuracy and data

rate, with respect to the only-radar configuration. In particular, the performance improvement is very drastic: angular accuracy is about 0.5° with respect to 1.7° of radar measurements, and data rate, gets to 5 Hz instead of 1 Hz provided by the radar sensor.

From off-line and HWIL analysis, also the multi-sensor intruder tracking has been worked out. Results have again confirmed benefits brought by EO sensors to the DS&A system, in fact multi-sensor tracking accuracy is one order of magnitude less than radar-only tracking. Next developments of that SAA project foresee to carry out multi-sensor intruder tracking during flight tests, in order to assess definitively that advantageous SAA UAV technology.

Further steps could consist in experimenting a SAA technology based on standalone EO sensors, because it would mean less weight and less costs of hardware and tests implementation. Moreover it would be suitable to a wider range of unmanned platforms, also micro UAV's. However, this study demands studying new image processing techniques, robust and reliable for a wide range of flight configurations.

References

[1]. Fabiani, P., "L'Autonomie Décisionnelle des Systèmes de drones : pour demain ? ", Résumé éntendu, ONERA

[2]. Ollero, A., Merino, L., "Control and perception techniques for aerial robotics", Annual Reviews in Control 28, 2004, 167 – 178

[3]. Lanillos, P., Ruz, J. J., Pajares, G., "Environmental surface boundary tracking and description using a UAV with vision", IEEE 2009

[4]. Kumar, M. P. S., Rajasekaran, S., "Detection and Extinguishing Forest Fires using Wireless Sensor and Actor Networks", International Journal of Computer Applications, Volume 24, No.1, June 2011

[5]. Redding, J., Amin, J., Boskovic, J. D., Jackson, J., "Collaborative Mission Planning Autonomy and Control Technology (CoMPACT) for Unmanned Surface Vehicles", AIAA Guidance, Navigation and Control Conference, Chicago, Illinois, 10 – 13 August, 2009

[6]. DeBusk, W. M., "Unmanned Aerial Vehicle Systems for Disaster Relief: Tornado Alley", AIAA Infotech@Aerospace 2010, Atlanta Georgia, 20 – 22 April, 2010

[7]. Dvorak, D. R., Semke, W. H., Neubert, J. J., Baer, N., Sorum, J. R., Schultz, R. R., "Evaluating the Performance of a UAS based Precision Agriculture Imaging Payload", AIAA Infotech@Aerospace 2010, Atlanta, Georgia, 20 – 22 April, 2010

[8]. US Federal Aviation Administration (FAA), "Airworthiness Certification of Unmanned Aircraft Systems", Order 8130.34, Washinton DC, USA, March 27th, 2008

[9]. US FAA, Order 7610.4K, "Special Military Operations", 2004

[10]. Maroney, D. R., Bolling, R. H., Athale, R., Christiansen, A. D., "Experimentally Scoping the Range of UAS Sense and Avois Capability", AIAA Infotech@Aerospace Conference, Ronhert Park, CA, May 2007

[11]. Rosenkrans, W., "Detect, Sense and Avoid", AeroSafety World Magazine, July 2008

[12]. Global Hawk ORD CAF 353-92-I/II-C, "Basic System for the Global Hawk Unmanned Aerial Vehicle (ROA) System", Air Force Command and Control & Intelligence, Surveillance, and Reconnaissance Center, September 2002

[13]. RQ-1 Predator ORD # CAF 003-90-I-A, 24 June 1997

[14]. Bergerman, M., Amidi, O., Miller, J. R., Vallidis, N., Dudek, T., "Cascaded Position and Heading Control of a Robotic Helicopter", Proceedings of the 2007 IEEE/RSJ International Conference on Intelligent Robots and Systems, San Diego, CA, USA, Oct 29 - Nov 2, 20074

[15]. Doherty, P., Kvarnström, J., Heintz, F., "A temporal logic-based planning and execution monitoring framework for unmanned aircraft systems", Springer Auton Agent Multi-Agent Syst, LLC 2009

[16]. Watanabe, Y., Lesire, C., Piquereau, A., Fabiani, P., Sanfourche, M., Le Besnerais, G., "The ONERA ReSSAC Unmanned Autonomous Helicopter : Visual Air-to-Ground Target Tracking in an Urban Environment", the American Helicopter Society 66th Annual Forum, Phoenix, Arizona, May 11-13, 2010

[17]. NATO NAVAL ARMAMENT GROUP, "SENSE AND AVOID REQUIREMENTS FOR UNMANNED AERIAL VEHICLE SYSTEMS OPERATING IN NON-SEGREGATED AIRSPACE", Document PFP(NNAG-LCGUAV)D(2008)0002, 23 April 2008

[18]. U.S. NTSB Public Forum, April 25, 2006

[19]. U.S. NTSB Public Forum, August 24, 2007

[20]. MTSI, July 2002, "Non-Cooperative Detect, See, & Avoid (DSA) Sensor Study," NASA ERAST technical report

[21]. ASTM Designation: F 2411 – 07, Standard Specification for Design and Performance of an Airborne Sense-and-Avoid System, ASTM International, West Conshohocken, PA, 2007

[22]. Smith, S. M., "ASSET-2: Real-Time Motion Segmentation and Object Tracking", Real-Time Imaging 4, 21–40 (1998)

[23]. Hwangbo, M., "Robust Monocular Vision-based Navigation for a Miniature Fixed-Wing Aircraft", PhD thesis at Carneige Mellon University, September 2009

[24]. Cesetti, A., Frontoni, E., Mancini, A., Zingaretti, P., Longhi, S., "A Vision-Based Guidance System for UAV Navigation and Safe Landing using Natural Landmarks", J Intell Robot Syst (2010) 57:233–257

[25]. Sanfourche, M., Le Besnerais, G., Fabiani, P., Piquereau, A., "Comparison of Terrain Characterization Methods for Autonomous UAVs", The American Helicopter Society 65th Annual Forum, Grapevine, Texas, May 27-29, 2009

[26]. Utt, J., McCalmont, J., Deschenes, M., "Development of a Sense and Avoid System," 1st AIAA Infotech@Aerospace Conference, Arlington, VA, 2005, pp- 1-10.

[27]. Gibbs, D.G., "Sense and Avoid Flight Demonstration," 2nd AIAA Infotech@Aerospace Conference and Exhibit, Paper 2007-2720, Rohnert Park, CA, 2007, pp 1-10.

[28]. Selier, M., Stuip, M., Verhoeven, R.P.M., "National Technology Project 'Outcast' on UAS Sense And Avoid," 26th International Congress of the Aeronautical Sciences ICAS, Anchorage, AL, 2008, pp. 1-10.

[29]. Shakernia, O., Chen, W. Z, Graham, S., Zvanya, J., White, A., Weingarten, N., Raska, V. M., "Sense and Avoid (SAA) Flight Test and Lessons Learned," 2nd AIAA Infotech@Aerospace Conference and Exhibit, Paper AIAA 2007-3003, Rohnert Park, CA, 2007, pp. 1-12.

[30]. Mejias, L., McNamara, S., Lai, J., Ford, J., "Vision-based detection and tracking of aerial targets for UAV collision avoidance," 2010 IEEE/RSJ International Conference on Intelligent Robots and Systems (IROS), 18-22 Oct. 2010, ISSN : 2153-0858 Print ISBN: 978-1-4244-6674-0, Digital Object Identifier : 10.1109/IROS.2010.5651028

[31]. Gandhi, T., Mau-Tsuen Yang, Kasturi, R., Camps, O., Coraor, L., McCandless, J., "Detection of obstacles in the flight path of an aircraft," IEEE Transactions on Aerospace and Electronic Systems, Volume: 39 , Issue: 1, Digital Object Identifier: 10.1109/TAES.2003.1188902, 2003 , Page(s): 176 – 191.

[32]. Dey, D., Geyer, C., Singh, S., Digioia, M., "Passive, Long-Range Detection of Aircraft: Towards a Field Deployable Sense and Avoid System," Field and Service Robotics, Vol. 62 (2010), pp. 113-123. doi:10.1007/978-3-642-13408-1_11

[33]. Fasano, G., Accardo, D., Moccia, A., Carbone, C., Ciniglio, U., Corraro, F., and Luongo, S. "Multi-Sensor-Based Fully Autonomous Non-Cooperative Collision Avoidance System for Unmanned Air Vehicles," AIAA Journal of Aerospace Computing, Information, and Communication, vol. 5, issue 10, 2008, pp. 338-360.

[34]. Korn, B., Edinger, C., "UAS in Civil Airspace: Demonstrating "sense and avoid" capabilities in flight trials," 27th Digital Avionics System Conference, St. Paul, MI, 2008, pp. 1-10.

[35]. Cornic, P., Garrec, P., Kemkemian, S., Ratton, L., "Sense and avoid radar using Data Fusion with other sensors," 2011 IEEE Aerospace Conference, 5-12 March 2011 ISSN: 1095-323X, Print ISBN: 978-1-4244-7350-2, DOI: 10.1109/AERO.2011.5747514.

[36]. Portilla, E., Fung, A., Chen, W.Z., Shakernia, O., and Molnar, T., May 2007, "Sense And Avoid (SAA) & Traffic Alert and Collision Avoidance System (TCAS) Integration for Unmanned Aerial Systems (UAS)," 2nd AIAA Infotech@Aerospace Conference and Exhibit, Paper AIAA 2007-3004, Rohnert Park, CA, 2007, pp 1-10.

[37]. Zeitlin, A.D., McLaughlin, M.P., "Safety of cooperative collision avoidance for unmanned aircraft," IEEE Aerospace and Electronic Systems Magazine, April 2007, Volume: 22, Issue:4 page(s): 9 ISSN : 0885-8985, DOI: 10.1109/MAES.2007.351714.

[38]. Accardo, D., Moccia, A., Cimmino, G., Paparone, L., "Performance Analysis and Design o fan Obstacle Detection and Identification System", 1st AIAA Infotech@Aerospace Conference, Arlington, VA, September 2005.

[39]. http://www.alliedvisiontec.com/emea/home.html

[40]. Fasano, G., Accardo, D., Moccia, A., Rispoli, A., "An Innovative Procedure for Calibration of Strapdown Electro-Optical Sensors Onboard Unmanned Air Vehicles", Sensors 2010, 10, 639-654; doi:10.3390/s100100639.

[41]. Jaklitsch, J.J.;Paturzo, "V.M. Non Line of Sight Boresight Based on Inertial Measurement Technology", In Proceedings of AUTOTESTCON IEEE Systems Readiness Technology Conference, Anaheim, CA, USA, September 22–25, 2003; pp. 527–533.

[42]. Wertz, J.R., Ed. Spacecraft Attitude Determination and Control; D. Reidel Publishing Company: Boston, MA, USA, 1978

[43]. Farrell, J.; Barth, M. The Global Positioning System and Inertial Navigation; McGraw-Hill: New York, NY, USA, 1999

[44]. Jain, R.; Kasturi, R.; Schunk, B. Machine Vision; Computer Science Series; McGraw-Hill: New York, NY, USA, 1995

[45]. Camera Calibration Toolbox for Matlab; Available online: http://www.vision.caltech.edu/bouguetj/calib_doc/ (Accessed on 20 October 2009).

[46]. Zhang, Z., "Flexible Camera Calibration by Viewing a Plane from Unknown Orientations", computer.org, ICCV 1999

[47]. Nisticò, W., "Segmentazione di Immagini in Tempo Reale per Robot Tetrapodi", tesi di laurea presso l' Università La Sapienza di Roma, A.A. 2001-2002

[48]. Ardizzone, E., "Teoria e Tecniche di Elaborazione dell'Immagine", 2000

[49]. Sonka, M., Hlavac, V., Boyle, R., Image Processing, Analysis, and Machine Vision, 1998.

[50]. Bruce, J., "Realtime machine vision perception and prediction", 2000.

[51]. Millet, P.T., "Vision-Based Precision Landings of a Tailsitter UAV", A thesis submitted to the faculty of Brigham Young University, April 2010

[52]. Russ, J.C., "The Image Processing Handbook", 2nd ed., Boca Raton, FL: CRC Press, 1995

[53]. Jain, R., Kashuri, R., Schunck, B.G., Edge Detection, Machine Vision, Chapter 5, pp. 140 – 185, Mc Graw – Hill, 1995

[54]. Ehsan Nadernejad, Sara Sharifzadeh, Hamid Hassanpour, "Edge Detection Techniques: Evaluations and Comparisons", Applied Mathematical Sciences, Vol. 2, 2008, no. 31, 1507 – 1520

[55]. Downey, G., A., "Electro-optical Tracking Considerations II", Proc. of SPIE Acquisition, Tracking and Pointing XVIII, Vol. 5082

[56]. Hwang, J., Huh, K., Lee, D., "Vision-based vehicle detection and tracking algorithm design", Optical Engineering 48(12), 127201 (December 2009).

[57]. Kazakova, N., Margala, M., Durdle, N.G., "Sobel edge detection processor for a real-time volume rendering

system", Circuits and Systems, 2004. ISCAS '04. Proceedings of the 2004 International Symposium on, 23-26 May 2004

[58]. Hanna, E. Straznicky, P. Goubran, R., "Obstacle Detection for Low Flying Unmanned Aerial Vehicles Using Stereoscopic Imaging", Instrumentation and Measurement Technology Conference Proceedings, 2008. IMTC 2008. IEEE, Victoria, BC, 12-15 May 2008

[59]. Sokalski, J., Breckon, T.P., Cowling,I., "Automatic Salient Object Detection In UAV Imagery", 25th International UAV Systems Conference, Bristol, UK, 2010

[60]. Li, Y., Olson, E.B., A General Purpose Feature Extractor for Light Detection and Ranging Data, Sensors 2010, 10, 10356-10375.

[61]. Haritaoglu, I., Harwood, D., Davis, L.S., 1999. Hydra: multiple people detection and tracking using silhouettes. International Conference on Image Analysis and Processing, Venice, Italy, 27 - 29 September 1999.

[62]. Beymer, D., McLauchlan, P., Coifman, B., Malik, J., 1997. A Real-time Computer Vision System for Measuring Traffic Parameters. IEEE Conference on Computer Society, San Juan, Puerto Rico, 17 - 19 June 1997.

[63]. Smith, S.M., Brady, J.M., 1995. ASSET-2: Real-Time Motion Segmentation and Shape Tracking. IEEE Transactions on pattern analysis and machine intelligence, Vol. 17, No. 8.

[64]. Shi, J., Tomasi, C. Good Features to Track. IEEE Conference on Computer Vision and Pattern Recognition, Seattle, June 1994.

[65]. Harris, C., Stephens, M. A COMBINED CORNER AND EDGE DETECTOR. Alvey Vision Conference, pp. 147–152. 1988

[66]. Frolova, D., Simakov, D., Matching with Invariant Features, The Weizmann Institute of Science, March 2004

[67]. Trajkovic, M., Hedley, M. Fast corner detection. Image and Vision Computing 16, p.75-87. 1988

[68]. Wang, H. and Brady, M. Real-time corner detection algorithm for motion estimation. Image and Vision Computing, vol. 13:9, pp. 695-703. 1995.

[69]. Seeger, U. and Seeger, R. Fast corner detection in grey-level image. Pattern Recognition Letters, Volume 15, Issue 7, pp. 669-675. 1994

[70]. Sanfourche, M., Le Besnerais, G., Fabiani, P., Piquereau, A., Whalley, M.S., Comparison of Terrain Characterization Methods for Autonomous UAVs, American Helicopter Society 65th Annual Forum, Grapevine, Texas, May 27-20, 2009.

[71]. Forlenza, L., Patrick Carton, P., Accardo, D., Fasano, G., Moccia, A., "A Fast Corner Detection Algorithm for Real-Time Target Detection Systems", paper submitted at *Sensors 2011,* under review

[72]. Yang, T., Zhang, Y., Shao, D., Li, Y., "Clustering method for counting passengers setting in a bus with single camera", Optical Engineering 49(3), 037203, March 2010

[73]. Gómez, J.R., Jaraba, E.H., Montañés, M.A., Contreras, F.M., Uruñuela, C.O., "Detection and classification of football players with automatic generation of models", Optical Engineering 49(1), 017005, January 2010

[74]. F. Girosi, A. Verri and V. Torre, "Constraints for the Computation of Optical Flow", IEEE Workshop on Visual Motion, Proceedings, pp:116-124, IEEE, 1989.

[75]. S.S. Beauchemin and J.L. Barron, "The Computation of Optical Flow", ACM Computing Surveys, Vol. 27, No. 3, pp: 433-461, 1995.

[76]. J.L. Barron, D.J. Fleet and S.S. Beauchemin, "Performance of Optical Flow Techniques", International Journal of Computer Vision, Vol. 12(1), pp. 43-77, 1993.

[77]. B.K.P. Horn and B.G. Schunck, Determining Optical Flow, Artificial Intelligence, Vol. 17, pp. 185-203, 1981.

[78]. Recchia, G., Fasano, G., Accardo, Moccia, A., Paparone, L., "An Optical Flow Based Electro-Optical See-and-Avoid System for UAVs", 1-4244-0525-4/07/$20.00 ©2007 IEEE.

[79]. Cutler, R., Turk, M., "View-based Interpretation of Real-time Optical Flow for Gesture Recognition", 1998 IEEE

[80]. Carnie, R., Walker, R., Corke, P., "Image Processing Algorithms for UAV "Sense and Avoid"", Proceedings of the 2006 IEEE International Conference on Robotics and Automation, Orlando, Florida - May 2006

[81]. Engelbrecht, R.J., Poe, C.M., Balke, K.N., "Development of a Distributed Hardware-In-The-Loop Simulation System for Transportation Networks", 78th Annual Meeting of the Transportation Research Board, January 1999

[82]. Adiprawita, W., Adang Suwandi Ahmad, A.S., Semibiring, J., "Hardware In The Loop Simulator in UAV Rapid Development Life Cycle", ICIUS 2007, Bali, Indonesia, Oct 24-25, 2007

[83]. Suwal, K.R., Chen, W., Molnar, T.C., "SeFAR Integration Test Bed for See and Avoid Technologies", Infotech@Aerospace, Arlington, Virginia, 26 - 29 September 2005

[84]. Forlenza, L., Fasano, G., Accardo, D., Moccia, A., "Laboratory Test Facility for Simulating a Sense and Avoid Flight System", AIAA Infotech@Aerospace Technical Conference, Atlanta, Georgia, USA, 20-22 April 2010

[85]. Forlenza, L., Fasano, G., Accardo, D., Moccia, A., Rispoli, A., "A HARDWARE IN THE LOOP FACILITY FOR TESTING MULTISENSOR SENSE AND AVOID SYSTEMS", 28th Digital Avionics Systems Conference, October 25-29, 2009, Orlando, FL, USA

[86]. Collinson, R.P.G., Introduction to Avionics, Microwave Technology Series 11, Chapan & Hall, 1996, pp. 324-327

[87]. Heikkilä, J., Silvén, O., "A Four-step Camera Calibration Procedure with Implicit Image Correction", Conference on Computer Vision and Pattern Recognition, 1997.

[88]. Stevens, M. R., Beveridge, J. R., Integrating graphics and vision for object recognition, Kluwer Academic, 2001, Appendix A

[89]. Pratt, W.K., Digital Image Processing, 2nd ed., Wiley Interscience, Mountain View, CA, USA, 1991, Part 5

[90]. G. Fasano, A. Moccia, D. Accardo, A. Rispoli, "Development and test of an Integrated Sensor System for Autonomous Collision Avoidance", 26th International Congress of the Aeronautical Sciences, Anchorage, AL, 2008

[91]. Fasano, G., Forlenza, L., Accardo, D., Moccia, A., Rispoli, A., "Integrated Obstacle Detection System based on Radar and Optical Sensors", AIAA Infotech@Aerospace Technical Conference, Atlanta, Georgia, USA, 20-22 April 2010

[92]. Forlenza, L., Fasano, G., Accardo, D., Moccia, A., "UAS Collision Avoidance System: Multi-Sensor Tracking Results", ATACCS'2011, 26-27 May 2011, Barcelona, Spain

[93]. Forlenza, L., Fasano, G., Accardo, D., Moccia, A., Rispoli, A., "Image Processing Algorithm for Integrated Sense And Avoid Systems", Proc. SPIE 7833, 78330R (2010); doi:10.1117/12.865085, Toulouse 20 - 23 September 2010

[94]. Fisher, R., Perkins, S., Walker, A., Welfar, E., "Thresholding", Hypermedia Image Processing Reference, 2003

[95]. Voorhees H, Poggio T, "Detecting textons and texture boundaries in natural images", Proc ICCV, 1987, pp 250–258.

[96]. Forlenza, L., Accardo, D., "Strategies for Improving the Electro-Optical Object Detection SW of an Integrated Sense and Avoid System", CEAS 2011 The International Conference of the European Aerospace Societies, 24 – 28 October 2011, Venice, Italy

[97]. Fasano, G., Forlenza, L., Tirri, A.E., Accardo, D., Moccia, A., "MULTI-SENSOR DATA FUSION: A TOOL TO ENABLE UAS INTEGRATION INTO CIVIL AIRSPACE", 30th Digital Avionics Systems Conference October 16-20, 2011, Seattle, WA.

[98]. Luongo, S., Di Vito, V., Fasano, G., Accardo, D., Forlenza, L., Moccia, A., "AUTOMATIC COLLISION AVOIDANCE SYSTEM: DESIGN, DEVELOPMENT AND FLIGHT TESTS", 30th Digital Avionics Systems Conference October 16-20, 2011, Seattle, WA